NASA CONTRACTOR REPORT

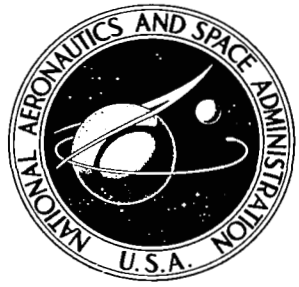

NASA CR-1341

EXPERIMENTAL INVESTIGATION IN AN ANNULAR CASCADE SECTOR OF HIGHLY LOADED TURBINE STATOR BLADING

Volume III. Performance of Tandem Blade

by James L. Bettner

Prepared by
GENERAL MOTORS
Indianapolis, Ind.
for Lewis Research Center

NATIONAL AERONAUTICS AND SPACE ADMINISTRATION • WASHINGTON, D. C. • MAY 1969

NASA CR-1341

EXPERIMENTAL INVESTIGATION IN AN ANNULAR CASCADE SECTOR OF HIGHLY LOADED TURBINE STATOR BLADING

Volume III. Performance of Tandem Blade

By James L. Bettner

Prepared under Contract No. NAS3-9404 by
GENERAL MOTORS
Indianapolis, Ind.

for Lewis Research Center

NATIONAL AERONAUTICS AND SPACE ADMINISTRATION

For sale by the Clearinghouse for Federal Scientific and Technical Information
Springfield, Virginia 22151 – CFSTI price $3.00

FOREWORD

The research described herein, which was conducted by the Allison Division of General Motors, was performed under NASA Contract NAS3-9404. The work was done under the technical management of Mr. Edward L. Warren and Mr. Stanley M. Nosek, Airbreathing Engines Division and Fluid System Components Division, respectively, NASA-Lewis Research Center. The report was originally issued as Allison EDR 5315, Volume III, May 1968.

TABLE OF CONTENTS

LIST OF TABLES

LIST OF ILLUSTRATIONS

EXPERIMENTAL INVESTIGATION IN AN ANNULAR CASCADE SECTOR OF HIGHLY LOADED TURBINE STATOR BLADING

Volume III. Performance of Tandem Blade

by J. L. Bettner

Allison Division of General Motors

SUMMARY AND CONCLUSIONS

A tandem blade consisting of two airfoils has been tested in a six-blade annular cascade. The performance of this blade has been evaluated and compared with that of a plain blade designed to the same set of velocity triangles and tested in the same cascade. The solidity of the tandem airfoil was approximately 91% of the plain blade.

By all modes of performance evaluation, the tandem blade met or exceeded the design requirements. Because of flow separation effects, the plain blade consistently fell short of satisfying the design requirements.

The tandem blade surface velocity distribution and blade loads agreed well with theoretical values. Suction surface diffusion factor requirements were met or exceeded.

High speed flow visualization studies showed that flow separation was prevented to the trailing edge of the tandem secondary airfoil. The tandem hub, mean, and tip blade sections were 1.2, 6.2, and 2.7%, respectively, in excess of satisfying the required change in tangential velocity across the blade row, while the comparable plain blade sections were 9.0, 8.5, and 11.1% deficient.

Loss calculations showed that loss levels for the tandem blade were about 15% less at the trailing edge (station 3) and 18% less two inches downstream of the trailing edge (station 4) than the plain blade.

From the comparison of the experimental values of the boundary layer shape factor (H) with the theoretical value required for flow separation at the trailing edge, the tandem blade of the present investigation could have been loaded even more heavily than it was before flow separation from the suction surface would have occurred. The tandem blade is a promising boundary layer control device on highly loaded turbine blades.

INTRODUCTION

Increasing interest in developing lightweight, highly loaded gas turbine engines confronts the designer with the problem of maintaining a high level of engine performance. A major cause of performance loss in present engines is the condition of the gas flow separating from the blading surfaces. When flow separation is experienced in a blade passage, there is a loss in available kinetic energy, mixing losses are increased, and the desired change in tangential momentum of the gas is not attained. The use of boundary layer control devices offers a possible means of preventing flow separation in maintaining performance in turbomachinery. The NASA Lewis Research Laboratory has contracted the Allison Division GMC to conduct an experimental research program to evaluate the aerodynamic performance of highly loaded turbine stator blades incorporating several kinds of boundary layer control devices. The following four concepts are being investigated:

- Vortex generators
- Tandem airfoils
- Jet-flapped blowing
- Tangential jet blowing

This report covers the performance evaluation of the tandem airfoil concept of boundary layer control. Blade surface static pressure and velocity distributions along with flow visualization results, aerodynamic loss, and boundary layer data are presented.

The analysis and design of all the blade configurations are presented in Volume I. The program base-line level of aerodynamic performance generated by a plain blade and subsequent evaluation of co-rotating vane and of triangular plow type vortex generators with respect to plain blade performance were established in Volume II. The aerodynamic performance of the jet-flapped and tangential jet blades is presented in Volumes IV and V, respectively.

SYMBOLS

A	area, $in.^2$
C_x	blade axial chord, in.
DS	region of gas turning from throat to trailing edge
Ds	suction surface diffusion factor, $1 - \frac{W/W_{cr})_2}{W/W_{cr})_{max}}$
$\bar{e}$	kinetic energy loss coefficient
F_y	tangential force, lb_f
H	boundary layer shape factor
$\dot{m}$	mass flow rate, lb_m/sec
P	pressure, psia
R	radial position, in.
s	blade spacing, in.
T	temperature, °R
W	velocity, ft/sec
β	gas angle measured from tangential, degrees
δ_o	ratio of inlet air total pressure to standard sea level conditions
δ^*	dimensionless boundary layer displacement thickness
θ^*	dimensionless boundary layer momentum thickness
Θ_{cr}	squared ratio of critical velocity at blade row inlet to critical velocity at standard sea level temperature
σ	blade solidity, C_x/s
ψ	gas angle measured from axial, degrees
$\bar{\omega}$	total pressure loss coefficient

Subscripts

o	station at stator inlet
1	station at blade throat
3	station immediately downstream of blade trailing edge
4	station two inches (measured in the axial direction) downstream of the blade trailing edge
∞	free stream conditions
cr	conditions of Mach number of unity
f	force

h	hub
i	incompressible
m	mass
p	primary
st	static
T	total

TANDEM BLADE PERFORMANCE

The tandem blade holds promise as an effective means of boundary layer control because it divides the required loading between multiple airfoils. In the present investigation, there were two airfoils—a primary and a secondary.

The six-blade annular cascade assembly of tandem airfoils is shown in Figure 1. The relative position of the primary and secondary airfoils with respect to each other and to the adjacent airfoils is shown in Figure 2. Blade number 3 was instrumented with static pressure taps primarily on the hub, mean, and tip section suction surface, while blade 4 was similarly instrumented on its pressure surface. This arrangement of static pressure taps permitted definition of the blade surface static pressure distribution through the center passage of the cascade. Design data for the tandem blade and the plain blade (which established the program base-line level of performance presented in reference 2) is given in Table I. The leading edges of blade numbers 1 and 6 were matched to a set of inlet guide walls, contoured to generate a free-vortex flow immediately upstream of the blade row. The plain blade was tested both with and without contoured exit guide walls that ducted the gas out of the rig. No exit guide walls were used in the tandem blade tests. Performance comparisons between the tandem and plain blades presented herein are based on the absence of exit guide walls on both blade configurations. Details of the guide walls and the test rig are given in reference 1. A photograph of the aft end of the test rig, with a plain blade mounted in position, is shown in Figure 3.

Information concerning the kind of instrumentation and associated accuracy is present in reference 1. Actual conduct of the test and data reduction procedure is delineated in reference 2.

VELOCITY AND PRESSURE DISTRIBUTIONS

Circumferential Static Pressure

Static pressure was measured by a series of pressure taps located on the hub and tip walls, 1/8-inch upstream and 1/8-inch downstream of the blade row. These taps were located on extensions of the midchannel streamline. The circumferential variation of hub and tip wall static pressure (nondimensionalized on the plenum total pressure) is presented in Figure 4 for the tandem blade and may be compared with the plain blade results in Figure 5. The degree of circumferential variation is nearly the same for both blade configurations. However, design free-vortex flow conditions existed at the trailing edge of the tandem blade, but were essentially absent at the plain blade trailing edge.

Blade Surface Velocity and Pressure Distributions

Measured and predicted surface velocity distributions on the hub, mean, and tip section tandem airfoils are presented in Figures 6, 7, and 8, respectively. The agreement between the measured and the predicted results is good, particularly at the mean section. The tandem blade design presented in reference 1 assumed a flow split for the main and slot channel of 73.6 and 26.4 percent of the total flow, respectively. The good agreement between the measured and predicted surface velocities in the slot region indicates that this flow split assumption was very reasonable.

The tandem blade was designed to prevent flow separation from the entire suction surface of both the primary and secondary airfoils. This resulted in the suction surface diffusion parameters shown in Table II. Similar data for the plain blade are also listed in Table II. These data are based on a constant total pressure through the stator. Since the actual distribution of total pressure through the stator was not known, the actual velocity at the trailing edge of the tandem blade primary airfoil could not be accurately computed. Therefore, the primary airfoil suction surface diffusion factor could not be determined. The most meaningful comparison between the tandem and plain blades would be to present the diffusion factor results on an isentropic velocity distribution basis. At nearly all radial positions on both the primary and secondary airfoils, the measured diffusion parameters for the tandem blade were considerably larger than the design values.

Examination of the velocity at the trailing edge of the secondary airfoil of Figures 6 through 8 shows that both the correct level and free-vortex distribution were achieved for the tandem blade. This was not the case for the plain blade, particularly at the hub section, as shown in Figures 9, 10, and 11.

The measured surface static pressure distribution, nondimensionalized on the inlet plenum total pressure, is illustrated in Figures 12, 13, and 14. A smooth curve was fitted through the experimental points, and the tangential blade load was computed. The results of the tandem and plain blade static pressure distribution force analysis are:

	Tangential force, F_y (lb_f)	Mass flow rate per passage $\dot{m}$ (lb_m/sec)	$F_y/\dot{m}$ (lb_f-sec/lb_m)
Tandem blade	40.950	1.360	30.11
Plain blade	31.86	1.240	25.69
Design value	31.33	1.05	29.80

These data are presented in Table III along with other experimental results. On a per pound mass of passage flow basis, the tandem blade loads were within 1% of the design value, while the plain blade was nearly 14% less than design. Both the tandem and plain blades were designed to be tested at the same inlet critical velocity $(W/W_{cr})_o$ conditions. These conditions are shown in Table I. As previously discussed, the inlet conditions were generated by a set of contoured inlet guide walls. However, because of geometrical differences in the leading edge region between the plain and tandem blades, a different set of inlet guide walls was required for each of the two blade configurations. These different sets of guide walls generated slightly different flow conditions immediately upstream of the blade rows. This is demonstrated by the radial distribution of inlet critical velocity ratio shown in Table III. The larger average inlet critical velocity ratio resulted in a slight increase in overall expansion ratio and actual flow rate for the tandem blade as compared with the plain blade.

FLOW VISUALIZATION RESULTS

Application of the lampblack-mineral oil flow visualization technique revealed that the tandem blade was quite successful in preventing flow separation. This result is demonstrated in Figures 15, 16, and 17. The flow rate through the cascade was varied from about 110, 100, and 90% of design conditions for Figures 15, 16, and 17, respectively. In nearly all cases, only a very thin line of separated flow was evident near the trailing edge. The flow was moving off the trailing edge in a very smooth fashion with neither strong radial or circumferential variation. This may be contrasted with the plain blade results which are shown in Figure 18 for the design flow conditions. The flow separated from the suction surface in Figure 18 and there was a combined radial-circumferential nonuniformity about the separated flow pattern.

DOWNSTREAM GAS ANGLE AND TANGENTIAL VELOCITY

Average Downstream Gas Angle Radial Distribution

A radial distribution of the measured average gas angle of blade numbers 3 and 4 of the cascade is shown in Figure 19. The theoretical distribution for a four-percent loss in total pressure across the cascade is also shown. The tandem blade turned the gas a considerably greater amount toward the tangential direction than the design value which was based on the assumed four-percent loss in total pressure across the cascade. A four-percent loss in total pressure, therefore, was not an accurate design assumption for this tandem blade. Some lesser amount of total pressure loss through the cascade should have been assumed. Similar plain blade results are shown

in Figure 20. In general, the plain blade did not achieve the correct radial distribution of downstream midchannel gas angle. This is in agreement with the plain blade flow visualization results which demonstrated that flow separation did occur. The gas left the blade suction surface before the required turning had been accomplished and, therefore, did not achieve the correct downstream gas angle distribution. For the tandem blade, flow separation did not occur to any degree before the trailing edge was reached, and the gas was turned an amount equal to or greater than the design value at all radial stations.

Change in Tangential Velocity Across Blade Row

Both the tandem and plain blades were designed to the same change in tangential velocity. Based on the inlet and exit critical velocity ratio, including loss and average downstream gas angle measurements, the experimental change in equivalent tangential velocity across the blade row was determined as follows:

	Experimental tandem blade, ΔW_u (ft/sec)	Experimental plain blade, ΔW_u (ft/sec)	Design value of ΔW_u (ft/sec)
Hub	1262.66	1136.01	1247.87
Mean	1090.95	940.59	1027.65
Tip	897.41	776.91	873.71

In all cases, the tandem blade exceeded while the plain blade fell short of satisfying the design change in tangential velocity requirements. From the surface velocity distribution plots, the flow visualization results, the radial distribution of the average downstream gas angle, and change in tangential velocity results, it appeared that the tandem blade had a level of performance not only superior to the plain blade but also exceeded the expected performance.

CONTOUR PLOTS

Results at the Blade Trailing Edge (Station 3)

As stated in reference 2, the total pressure surveys were performed at 10 radial depths immediately downstream of and encompassing the wakes of blade numbers 3 and 4. From these survey data, circumferential distributions of kinetic energy and total pressure loss coefficient were computed. An example of these data and results for one radial position (R = 13.01 inch) is shown in Figures 21 and 22 for the tandem blade. Similar

results are shown for the plain blade at about the same radial position in Figures 23 and 24. It is demonstrated in Figures 22 and 24 that tandem blade loss at the radial depth in question is markedly less than that for the plain blade. The loss level for the tandem blade was reduced with respect to the plain blade over the whole radial span, except near the hub section. This is demonstrated in the kinetic energy and total pressure loss contour plots of Figures 25 and 26. The plain blade kinetic energy loss contour plot is shown in Figure 27. It is quite obvious from Figures 25 and 27 that the high loss region for the tandem blade is not only reduced in size but also in level when compared with the plain blade.

Results Downstream of the Blade Trailing Edge (Station 4)

Kinetic Energy Loss Coefficient

Contours of kinetic loss coefficient are presented in Figures 28 and 29 for the tandem and plain blades, respectively. The highly skewed appearance of the loss contours of Figure 28 is a result of the large amount of turning from the axial direction. The loss contours of Figure 29 show a fairly strong variation in the circumferential direction. This is not so evident in Figure 28 with the tandem blade loss being quite uniform from blade wake to blade wake.

Downstream Gas Angle

Contour plots of the gas angle, measured from the axial direction, two inches downstream of the trailing edge are shown in Figures 30 and 31 for the tandem and plain blades. The theoretical distribution for the gas angle, based on a four percent loss in total pressure across the cascade, is presented as the right hand ordinate of Figures 30 and 31. The consistent overturning of the gas from the axial direction is apparent in Figure 30 for the tandem blade. The only region in which the plain blade experienced design or overdesign turning was near the hub section.

MASS AVERAGED LOSS AND BOUNDARY LAYER PARAMETERS

Results at the Blade Trailing Edge (Station 3)

Circumferentially mass averaged values of the kinetic energy and total pressure loss coefficients were computed at each radial depth surveyed by equations 6 and 9 of reference 2. The numerical integrations were performed in the circumferential direction encompassing the points of minimum total pressure in the wakes of blade numbers 3 and 4.

The kinetic energy loss coefficient results for the tandem and plain blades are shown in Figures 32 and 33. The tandem blade radial distribution of

circumferentially mass averaged total pressure loss coefficient is shown in Figure 34. It is evident from Figures 32 and 33 that the loss level for the tandem blade is considerably reduced from that of the plain blade, except near the hub section. An overall flow passage mass averaged value of loss was computed at the trailing edge of the tandem blade and is compared with similar results for the plain blade as follows:

	Kinetic energy loss coefficient, $\bar{e}$	Total pressure loss coefficient, $\bar{\omega}$
Tandem blade	0.0772	0.0901
Plain blade	0.0959	0.1061

These results, which are included in Table III with other experimental data, demonstrate that the tandem blade effected a 19.5% reduction in $\bar{e}$ and a 15.1% reduction in $\bar{\omega}$ with respect to the plain blade loss levels in the trailing edge region.

The boundary layer parameters δ^*, θ^*, and H were computed from equations 11, 12, and 13 of reference 2. The radial distribution of the tandem blade results are illustrated in Figures 35, 36, and 37, while the radial distribution of the plain blade shape factor (H) is included as Figure 38. In general, δ^* and θ^* are radially uniform and have small values, indicating a uniform flow from the trailing edge with little energy loss or boundary layer blockage effects.

The curves of most interest, however, are the radial variations of the boundary layer shape factor for the tandem and plain blades. These results are shown in Figures 37 and 38, respectively. Figure 37 shows that H for the tandem blade is quite uniform with a value of about 1.25. Similar plain blade results show much larger values with large radial variations in magnitude.

To determine how close the flow was to separating from the blade, it was necessary to compute the magnitude of H that should exist for flow separation to occur with the levels of trailing edge critical velocity ratio shown in Figures 6, 7, and 8. Using equation 14 of reference 2 with $H_i = 1.8$ and $T_{T_\infty}/T_{st_3} \approx 1.075$ at the hub and 1.012 at the tip indicated that H should vary from about 2.0 at the hub to 2.1 at the tip to have incipient flow separation at the blade trailing edge. Figure 37 shows that considerable margin remains before the tandem airfoil would experience flow separation.

Using the same critiera for separation, the plain blade should experience separation on the outer half of the airfoil as indicated in Figure 18.

The tandem blade, therefore, did not experience flow separation before the trailing edge was reached and could have been loaded more heavily before separation of the flow from the suction surface would have occurred.

Results Downstream of the Trailing Edge (Station 4)

Boundary layer parameters and circumferentially mass averaged loss coefficients were computed at each of the 10 surveyed radial positions two inches downstream of the blade trailing edge. These results are presented in Figures 39 through 45, with Figures 40 and 45 being plain blade results included for comparison purposes.

Examination of Figures 39 through 41 shows that the tandem blade had considerably lower loss levels over nearly the complete blade span, except near the hub section. This effect is attributed to the flow separating off of the hub casing wall at this axial location. Figures 19 and 30 show that the tandem blade accomplished greater turning (from axial) than did the plain blade. The flow was turned more toward the tangential direction and, therefore, was more susceptible to separation from the hub casing wall.

Even though the performance evaluation is somewhat clouded by having the flow separate from the hub casing wall, overall mass overaged loss coefficients were computed for this axial station as follows:

	$\bar{e}$	$\bar{\omega}$
Tandem blade	0.0925	0.1066
Plain blade	0.1133	0.1308

These results, included in Table III, show that at station 4 the tandem blade effected an 18.35% reduction in $\bar{e}$ and an 18.5% reduction in $\bar{\omega}$ with respect to the plain blade loss values.

Boundary layer parameters for axial station 4 are presented in Figures 42, 43, and 44 for the tandem blade. Figure 45, which is the plain blade radial distribution of shape factor, is included for comparison purposes. δ^* and θ^* are measures of boundary layer blockage and energy loss effects. Figures 42 and 43 show that these effects are very small in the mid-span region of the blade with a moderate increase in the tip region. They are, however, quite large near the hub which is in keeping with the conclusion that the flow separated from the hub casing wall.

The radial distribution of the tandem blade boundary layer shape factor in Figure 44 shows a nearly constant value of about 1.15 to 1.20 except at

the hub where it is over 4.0. As indicated in reference 2 for the loss level that existed at station 4 for the plain blade, H should be radially uniform with a value of 1.258 for complete mixing to have occurred. Figure 45 shows a nearly radially uniform value of 1.25. If the loss level decreases, then the value of H for complete mixing also decreases. This result is demonstrated in Figure 44 for the tandem blade.

SUMMARY OF TANDEM BLADE PERFORMANCE

From the experimental results presented in this investigation, it is concluded that the tandem blade holds real promise as a boundary layer control device on highly loaded turbine blades. In nearly every mode of performance evaluation, the tandem blade met or exceeded design conditions. These performance evaluations were as follows.

- The agreement between measured and predicted surface velocity and pressure distributions was quite good.

- The design suction surface diffusion factor was either met or considerably exceeded by the test results. These results are presented in Table II.

- The measured blade loads agreed well with the theoretical value, while the load on a plain blade designed to the same velocity triangles was considerably less than the theoretical value. The solidity of the tandem blade was about 0.91 of the plain blade.

- Flow visualization studies revealed that flow separation was essentially prevented all the way to the blade trailing edge.

- The tandem blade exceeded while the plain blade was deficient in achieving the required change in tangential velocity across the blade row. The results of measured and predicted change in equivalent tangential velocity across the blade row are:

	Tandem blade (ft/sec)	Plain blade (ft/sec)	Design values (ft/sec)
Hub	1262.66	1136.01	1247.87
Mean	1090.95	940.59	1027.65
Tip	897.41	776.91	873.71

- The loss levels for the tandem blade were about 15% less at the trailing edge (station 3) and 18% less at station 4 than the plain blade which was designed to the same velocity triangles. The computed value of overall mass averaged loss coefficients were:

	Station 3		Station 4	
	$\overline{e}$	$\overline{\omega}$	$\overline{e}$	$\overline{\omega}$
Tandem blade	0.0772	0.0901	0.0925	0.1066
Plain blade	0.0959	0.1061	0.1133	0.1308

REFERENCES

1. Bettner, J. L.: Experimental Investigation in an Annular Cascade Sector of Highly Loaded Turbine Stator Blading. vol. I, Analysis and Design. NASA CR-1219, 1968.

2. Bettner, J. L.: Experimental Investigation in an Annular Cascade Sector of Highly Loaded Turbine Stator Blading. vol. II, Performance of Plain Blade and Effect of Vortex Generators. NASA CR-1323, 1969.

Table I.

Design data for tandem and plain blades.

		Tandem blade			Plain blade		
	Units	Hub	Mean	Tip	Hub	Mean	Tip
C_x	in.	1.2290	1.4555	1.6835	1.3650	1.5925	1.8200
s	in.	1.01267	1.22967	1.44678	1.01267	1.22967	1.44678
σ		1.213	1.185	1.164	1.348	1.293	1.258
β_o	degrees	36.08	41.66	46.37	36.08	41.66	46.37
ψ_1	degrees	46.85	42.02	37.73	47.85	43.02	38.73
DS turning	degrees	15.0	15.0	15.0	13.0	13.0	13.0
$W/W_{cr})_o$		0.703	0.623	0.572	0.703	0.623	0.572
$W/W_{cr})_4$		0.799	0.707	0.647	0.799	0.707	0.647

Table II.

Experimental and design values of suction surface diffusion factors for the tandem and plain blades.

(Based on an isentropic surface velocity distribution)

	Tandem blade				Plain blade	
	Primary airfoil		Secondary airfoil			
	Design	Measured	Design	Measured	Design	Measured
Hub	0.114	0.238	0.226	0.225	0.400	0.330
Mean	0.150	0.286	0.221	0.250	0.400	0.332
Tip	0.185	0.248	0.232	0.350	0.400	0.312

Table III.

Experimental results for the tandem and plain blades.

	Tandem blade	Plain blade
Kinetic energy loss coefficient		
Exit plane (Station 3)	0.0772	0.0959
Downstream plane (Station 4)	0.0925	0.1133
Total pressure loss coefficient		
Exit plane (Station 3)	0.0901	0.1061
Downstream plane (Station 4)	0.1066	0.1308
Actual flow rate, lb_m/sec	1.360	1.240
Equivalent flow rate, lb_m/sec	1.088	0.996
Tangential blade force per pound mass of passage flow, lb_f-sec/lb_m	30.11	25.69
Plenum total pressure (P_{T_o}), in. Hg abs	38.515	37.481
Barometric pressure (P_{Baro}), in. Hg abs	29.115	29.306
$P_{T_o}/P_{st_{4h}}$	1.360	1.288
P_{T_o}/P_{Baro}	1.323	1.279
Plenum total temperature (T_{T_o}), °R	550.0	525.0
Θ_{cr}	1.060	1.012
δ_o	1.287	1.253
Inlet W/W_{cr}, ft/sec		
Hub	0.704	0.703
Mean	0.650	0.633
Tip	0.599	0.559
Change in equivalent tangential velocity across blade row, ft/sec		
Hub	1262.66	1136.01
Mean	1090.95	940.59
Tip	897.41	776.91

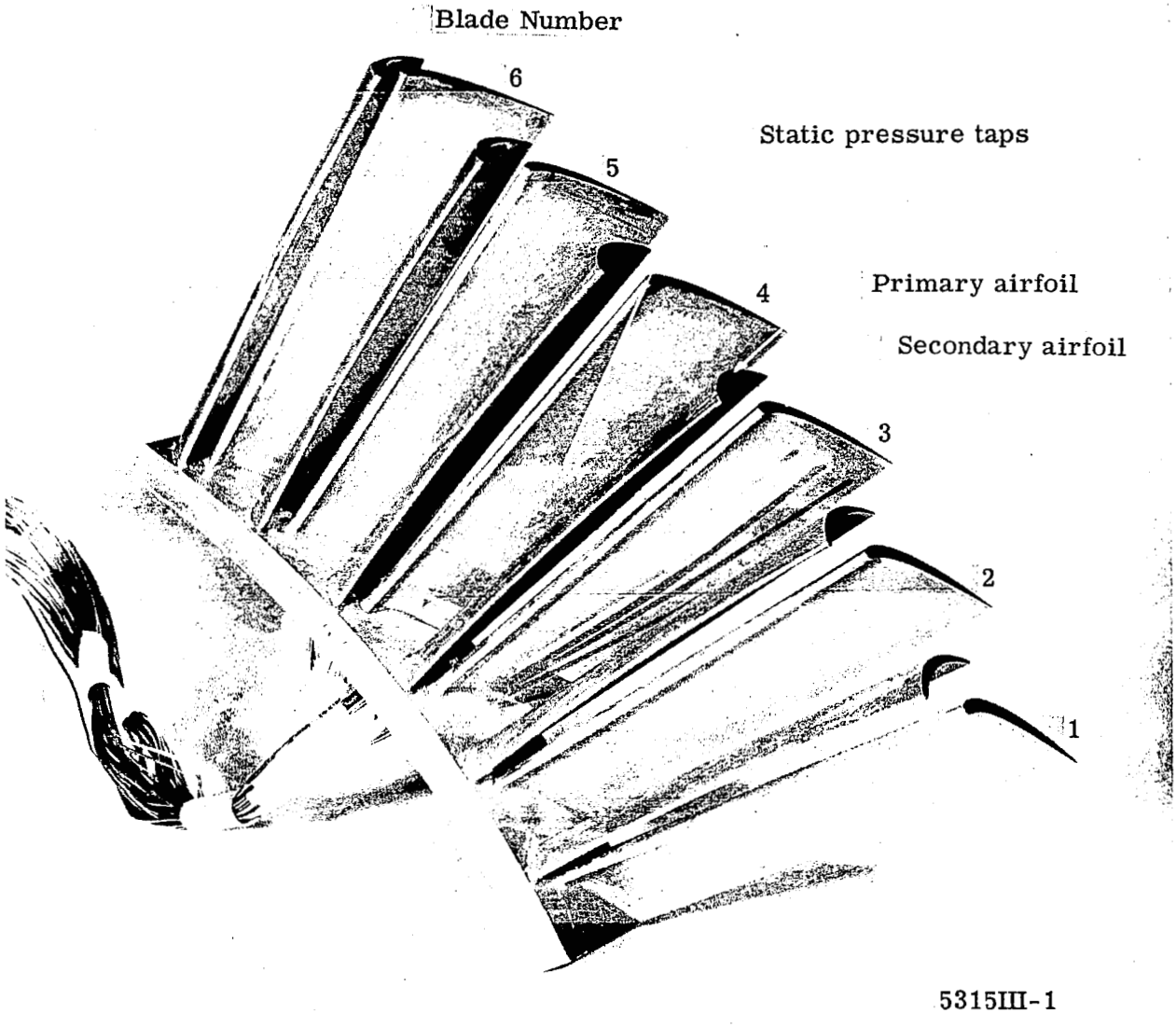

Figure 1. Tandem airfoil blade assembly.

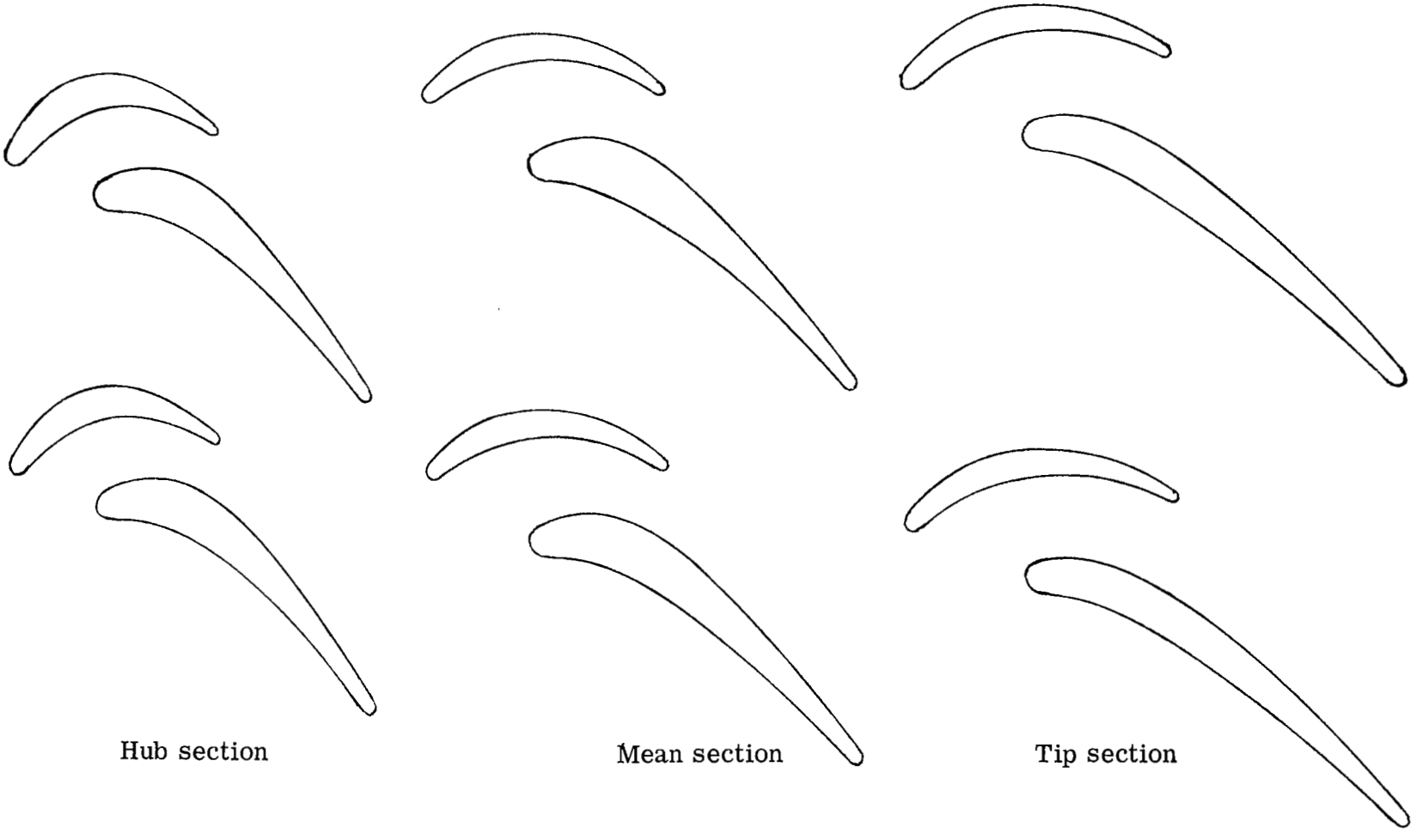

Figure 2. Tandem blade profiles and passages.

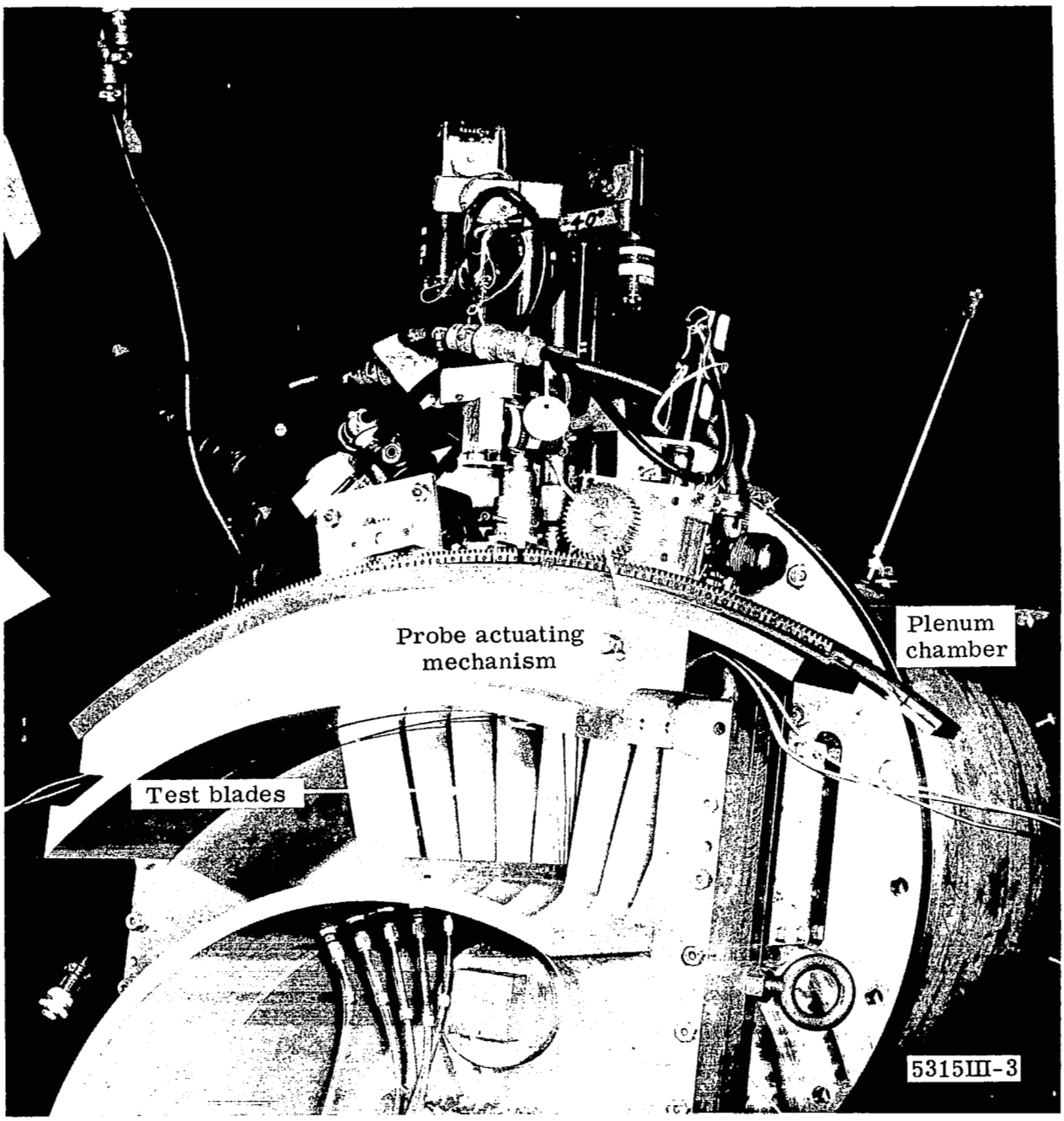

Figure 3. Annular cascade test rig.

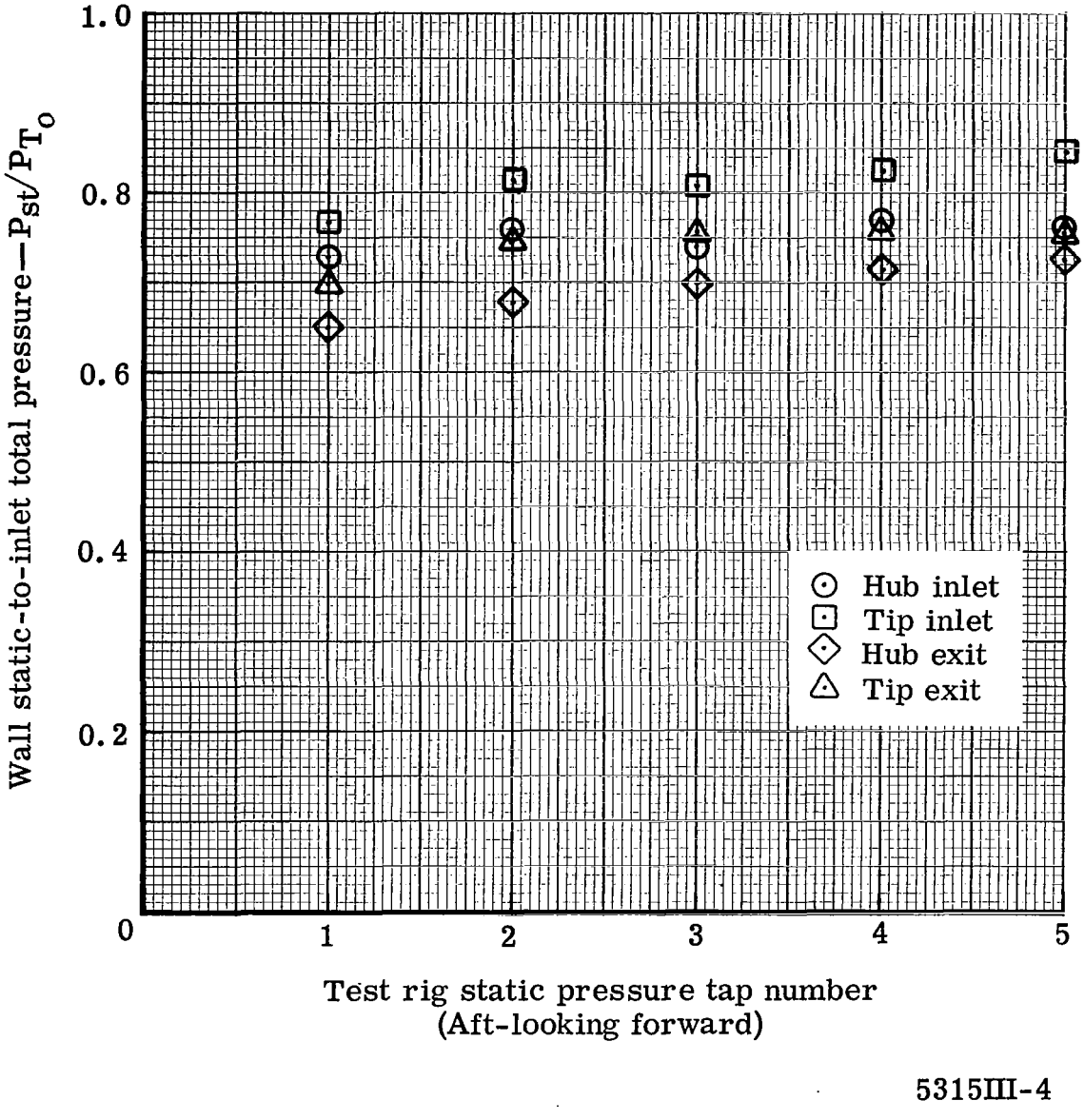

Figure 4. Circumferential variation of static pressure on inlet and exit hub and tip walls for tandem blade.

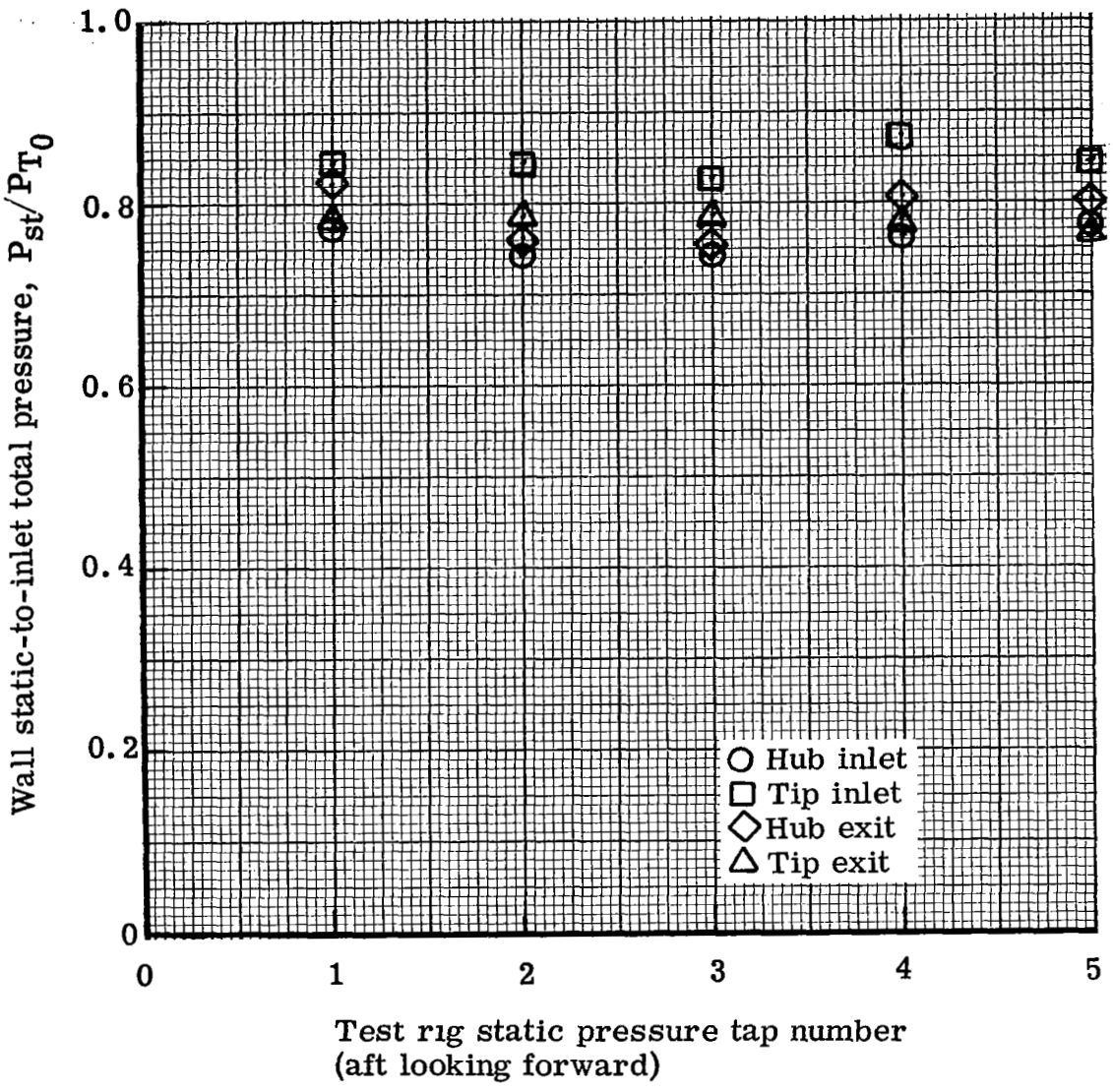

Figure 5. Circumferential variation of static pressure on inlet and exit hub and tip walls for plain blade.

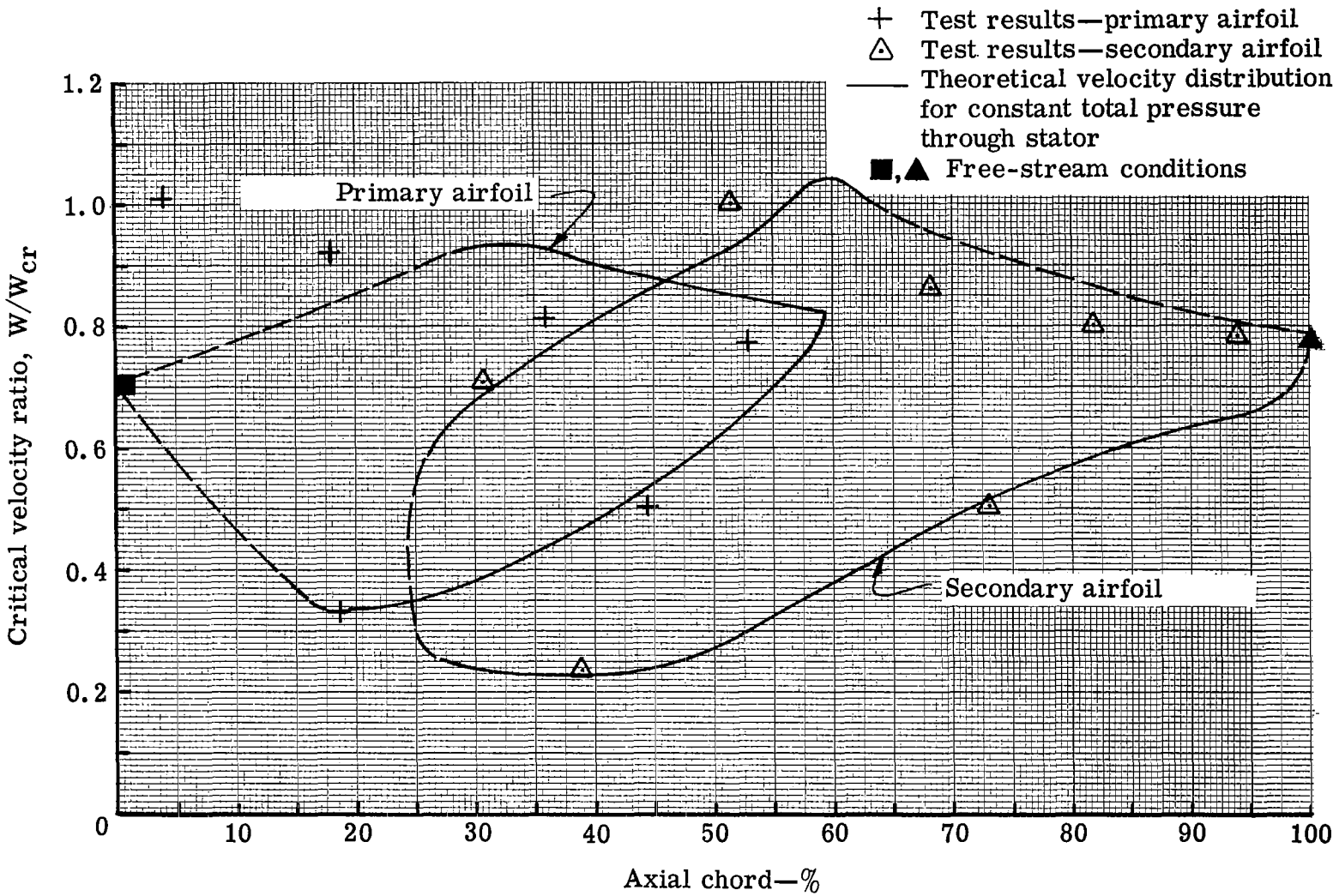

Figure 6. Measured and predicted surface critical velocity ratio distribution for tandem blade hub section.

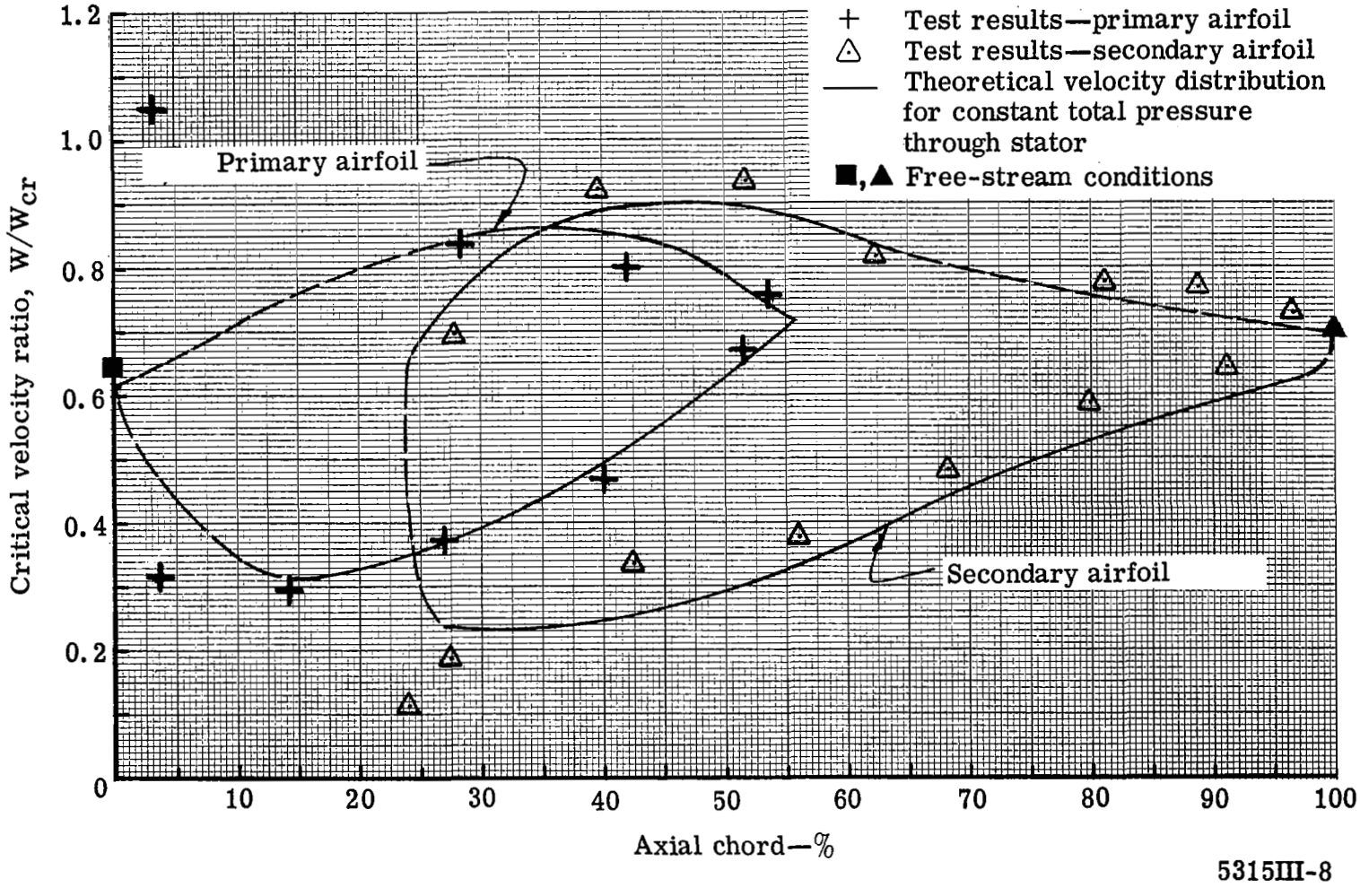

Figure 7. Measured and predicted surface critical velocity distribution for tandem blade mean section.

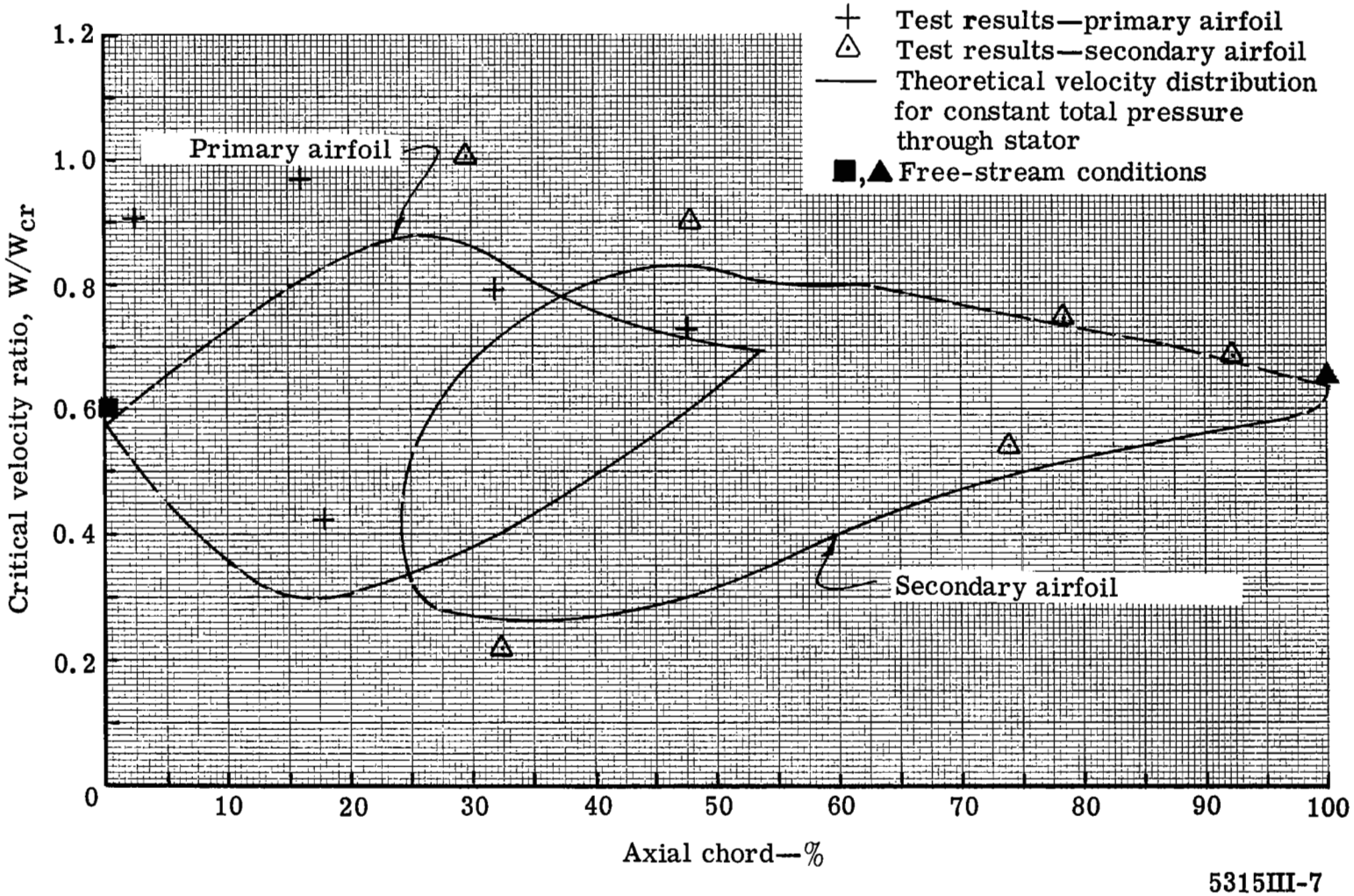

Figure 8. Measured and predicted surface critical velocity distribution for tandem blade tip section.

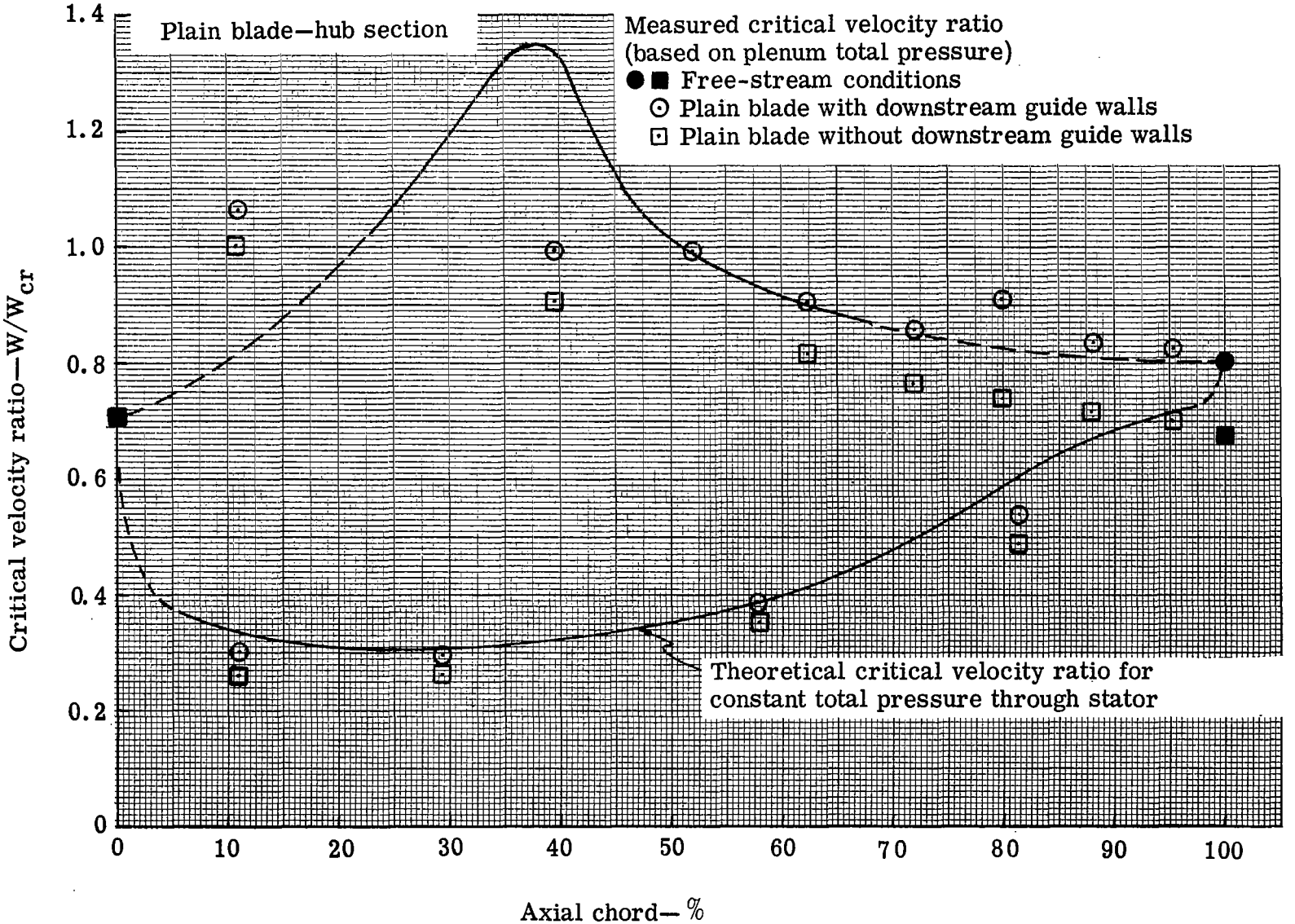

Figure 9. Measured and predicted surface critical velocity ratio distribution for plain blade hub section.

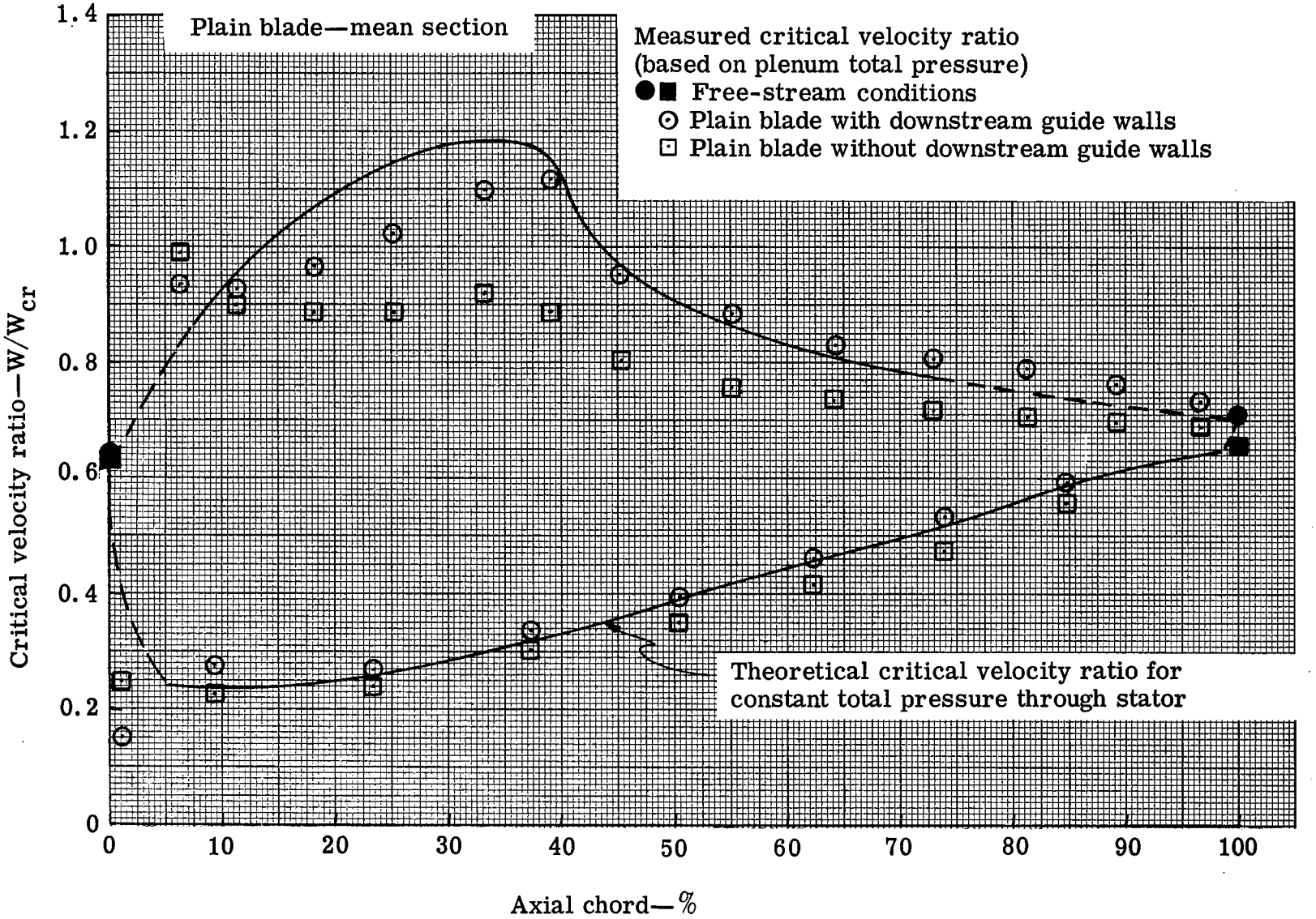

Figure 10. Measured and predicted surface critical velocity ratio distribution for plain blade mean section.

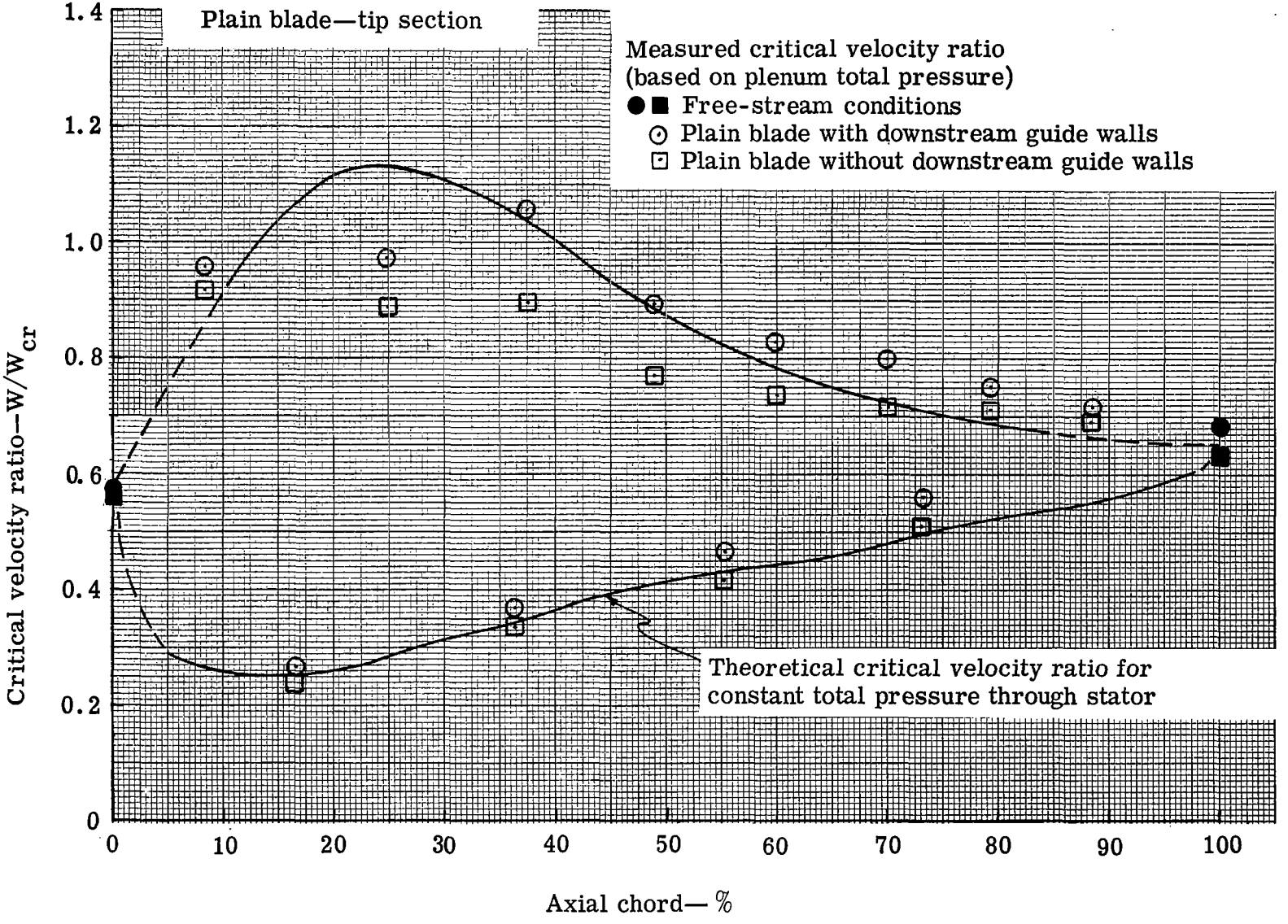

Figure 11. Measured and predicted surface critical velocity ratio distribution for plain blade tip section.

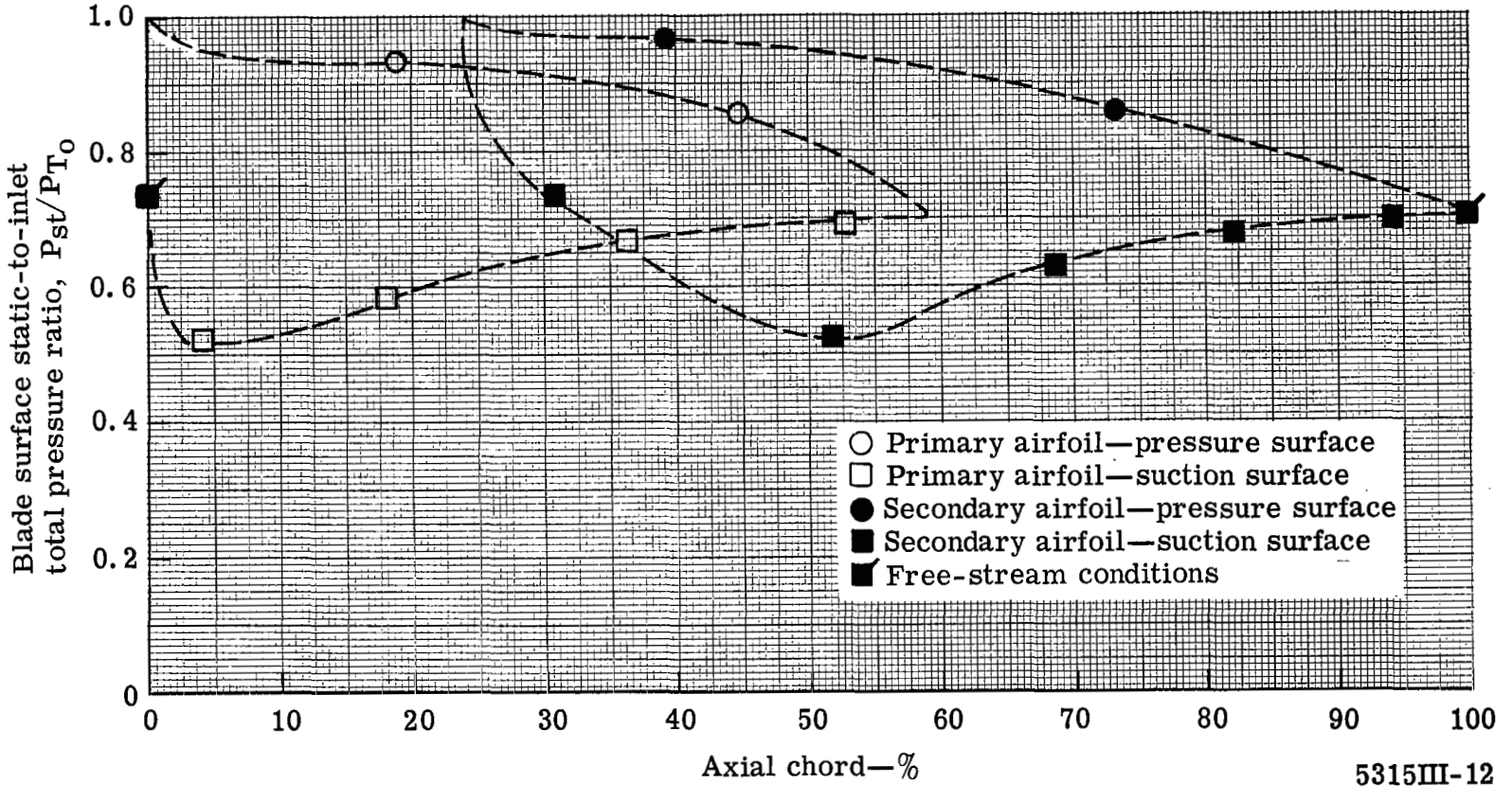

Figure 12. Measured surface static pressure distribution for the tandem blade hub section.

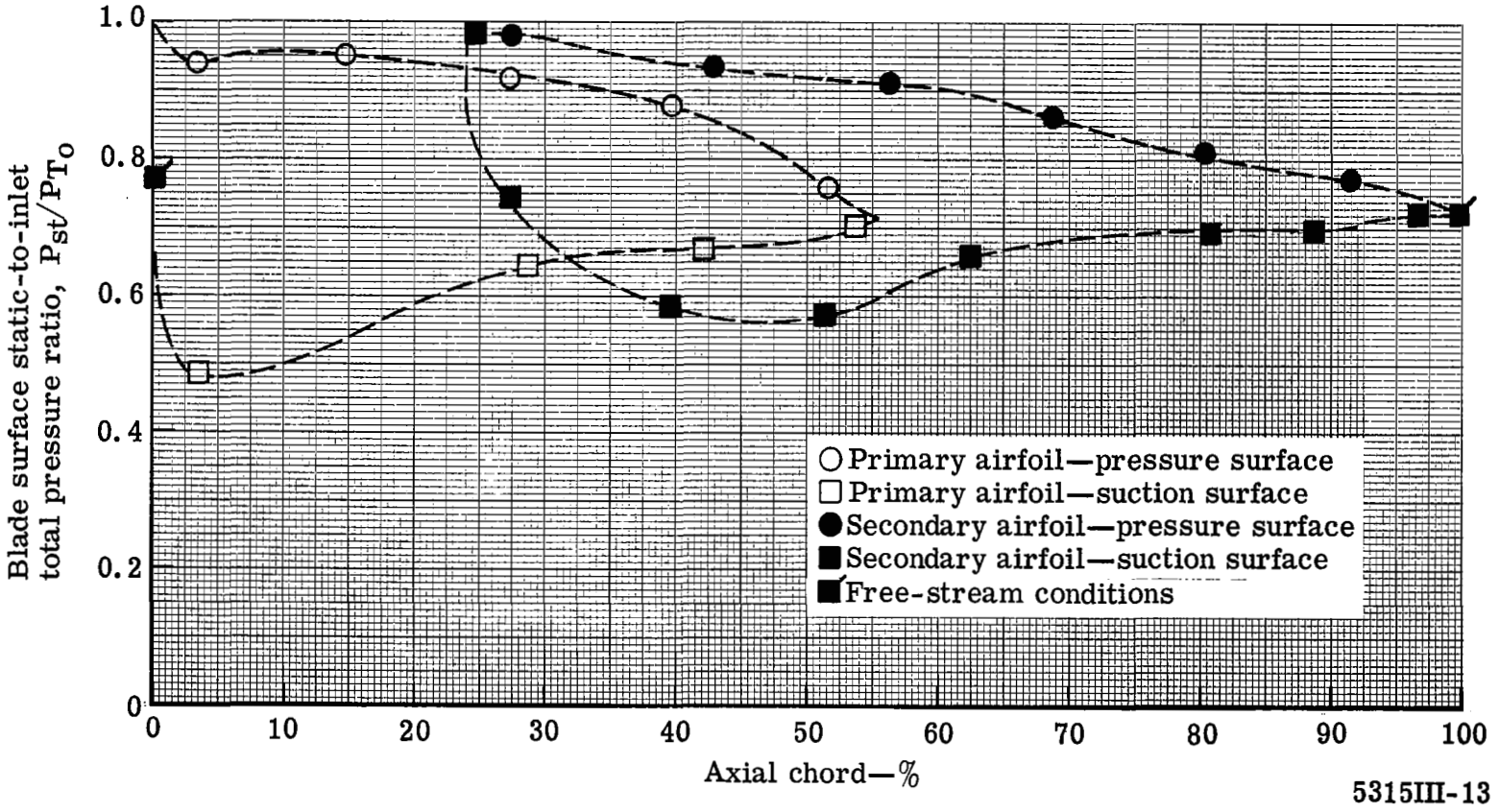

Figure 13. Measured surface static pressure distribution for the tandem blade mean section.

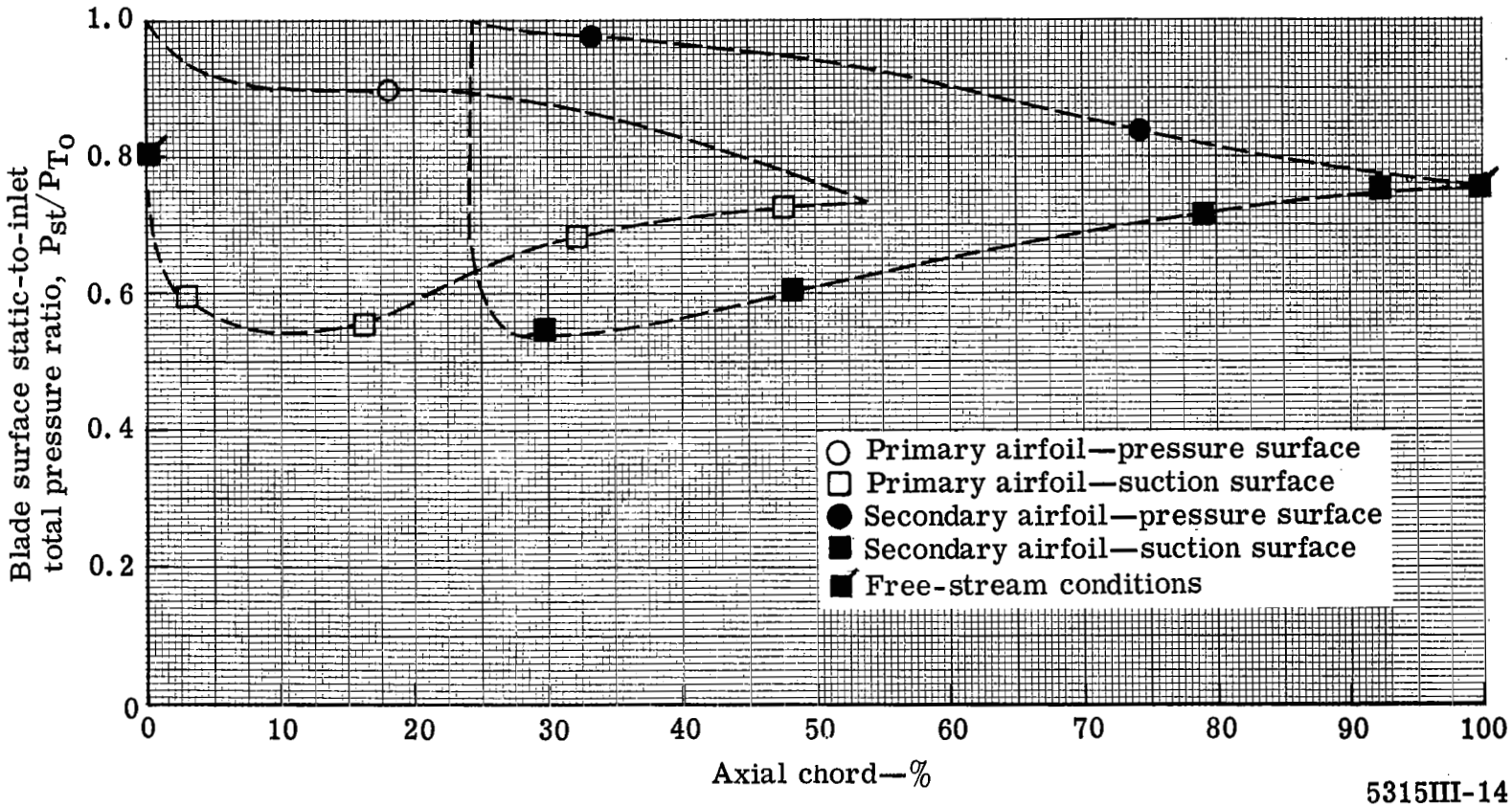

Figure 14. Measured surface static pressure distribution for the tandem blade tip section.

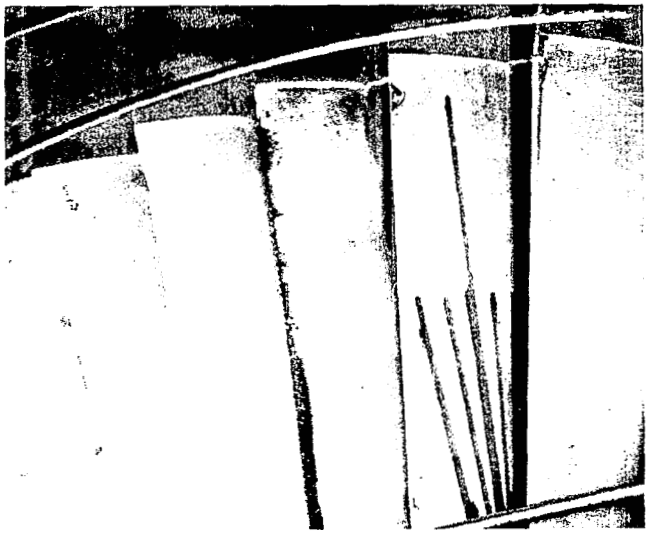

Vane No. 3

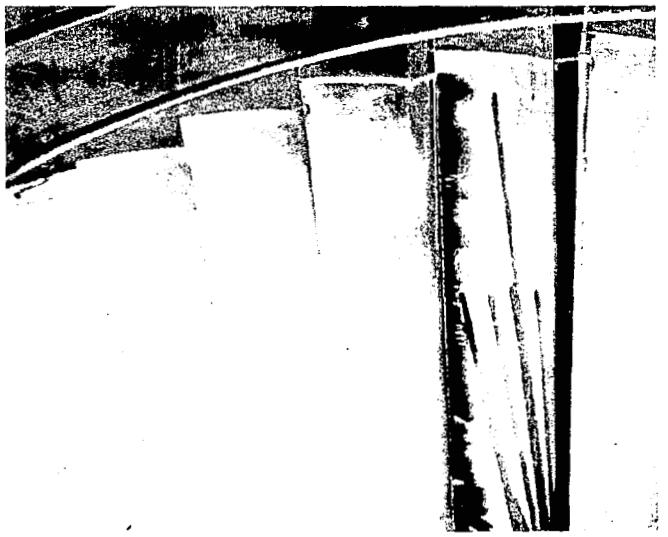

Vane No. 4

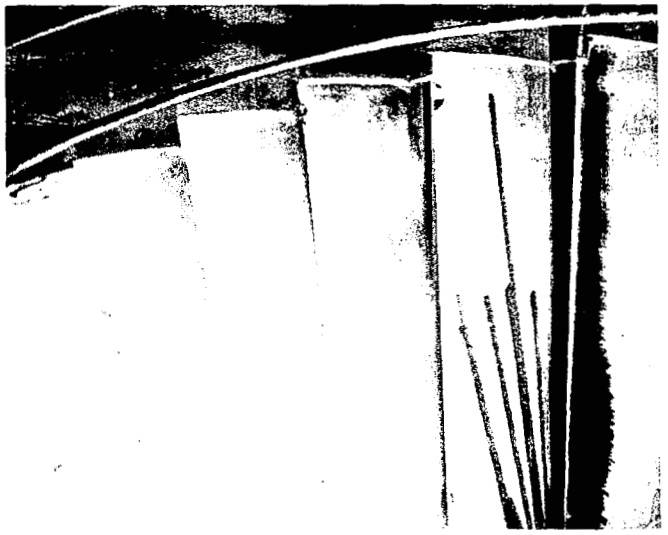

Vane No. 5

Figure 15. Tandem blade flow visualization results for inlet hub static-to-total pressure ratio of 0.65 (below design value).

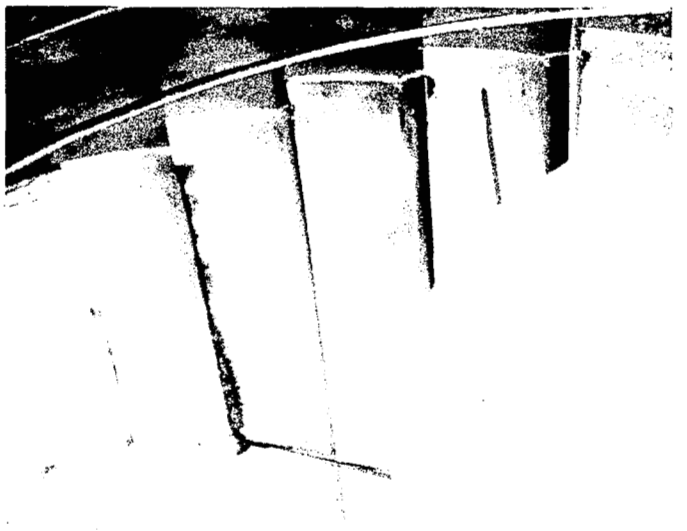

Vane No. 2

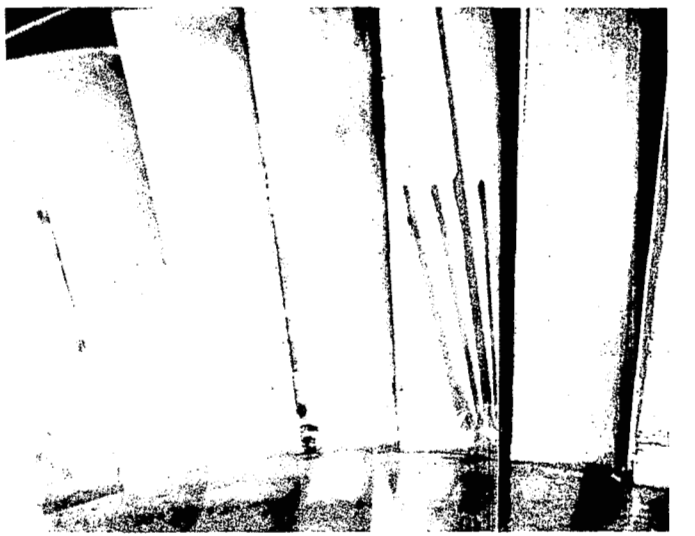

Vane No. 3

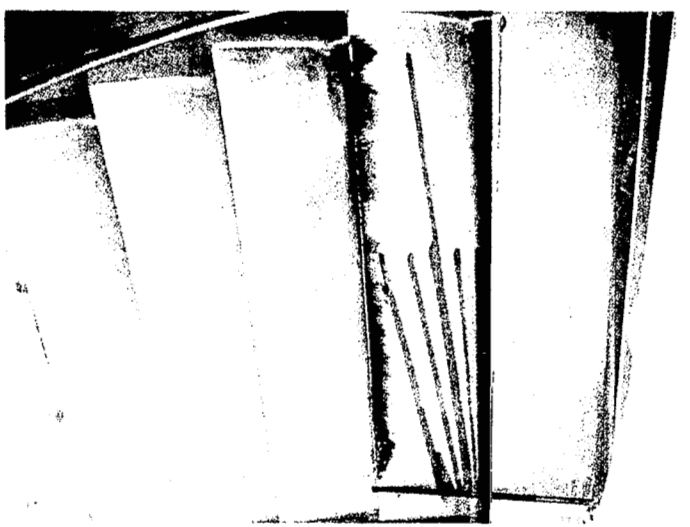

Vane No. 4

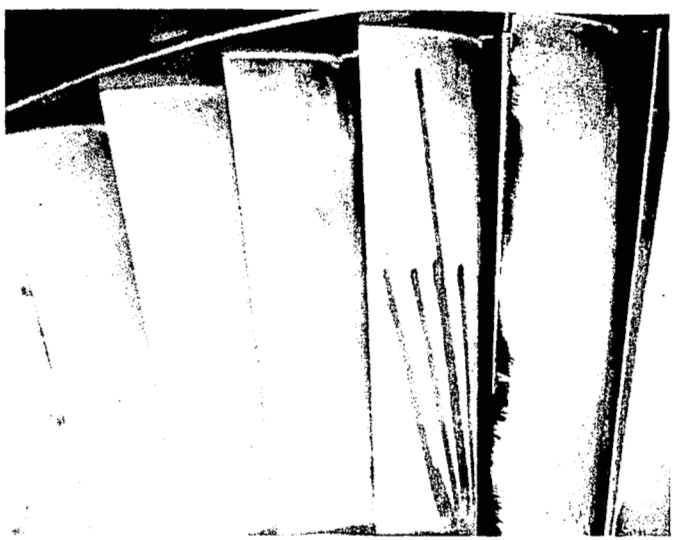

Vane No. 5

Figure 16. Tandem blade flow visualization results for inlet hub static-to-total pressure ratio of 0.74 (design value).

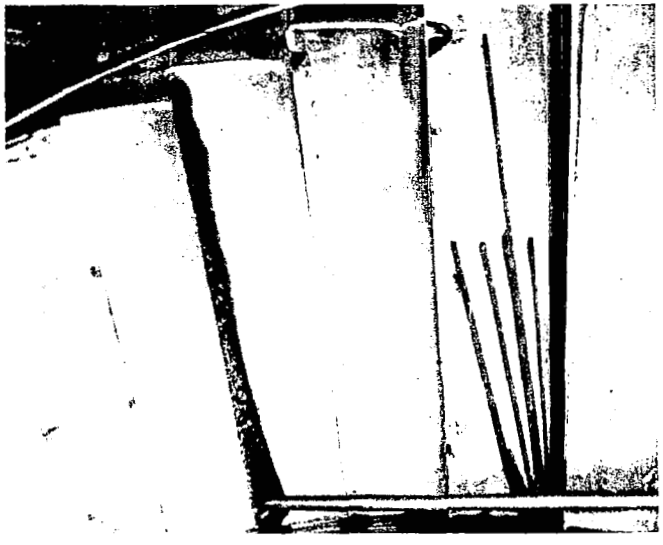

Vane No. 2

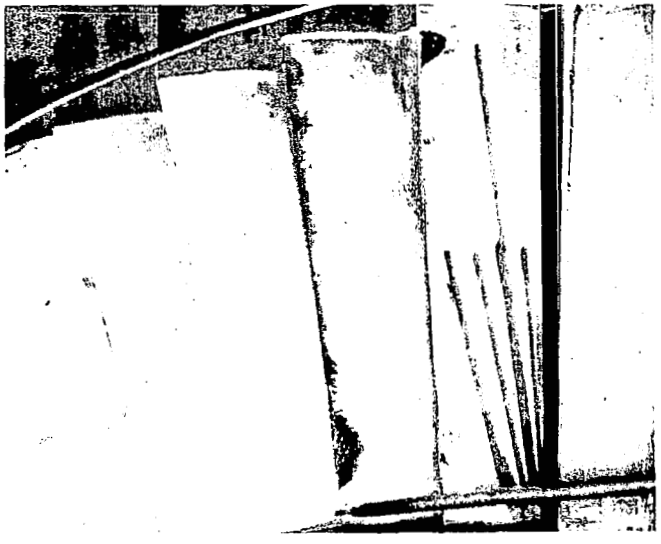

Vane No. 3

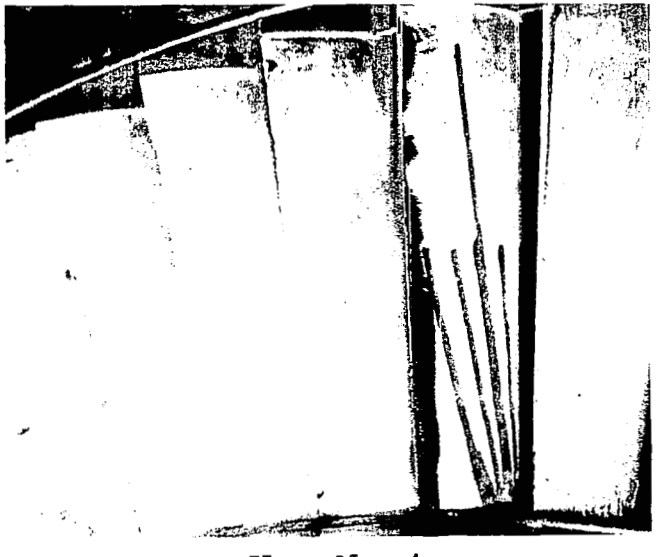

Vane No. 4

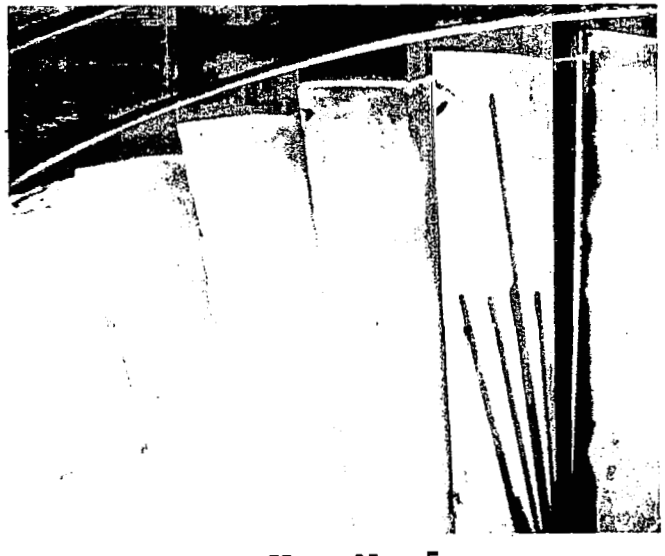

Vane No. 5

Figure 17. Tandem blade flow visualization results for inlet hub static-to-total pressure ratio of 0.82 (above design value).

Vane No. 2

Vane No. 3

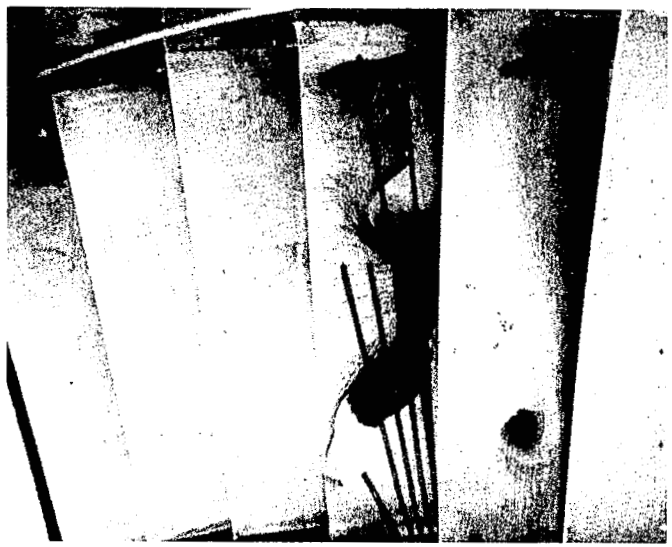

Vane No. 4

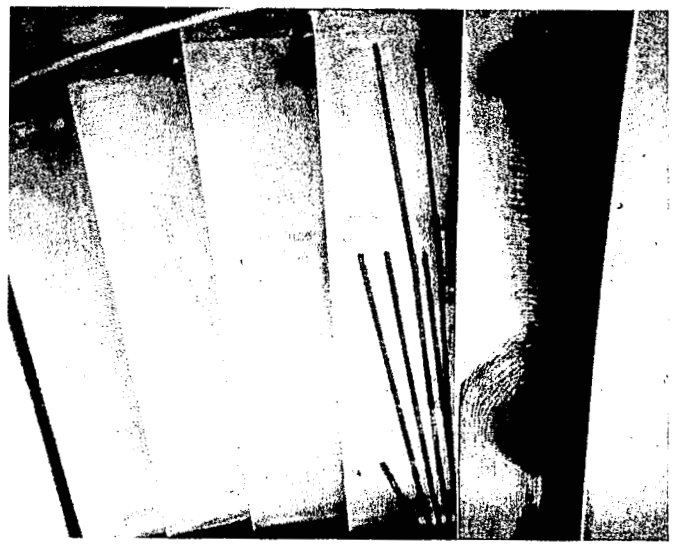

Vane No. 5

Figure 18. Plain blade flow visualization results for inlet hub static-to-total pressure ratio of 0.74 (design value).

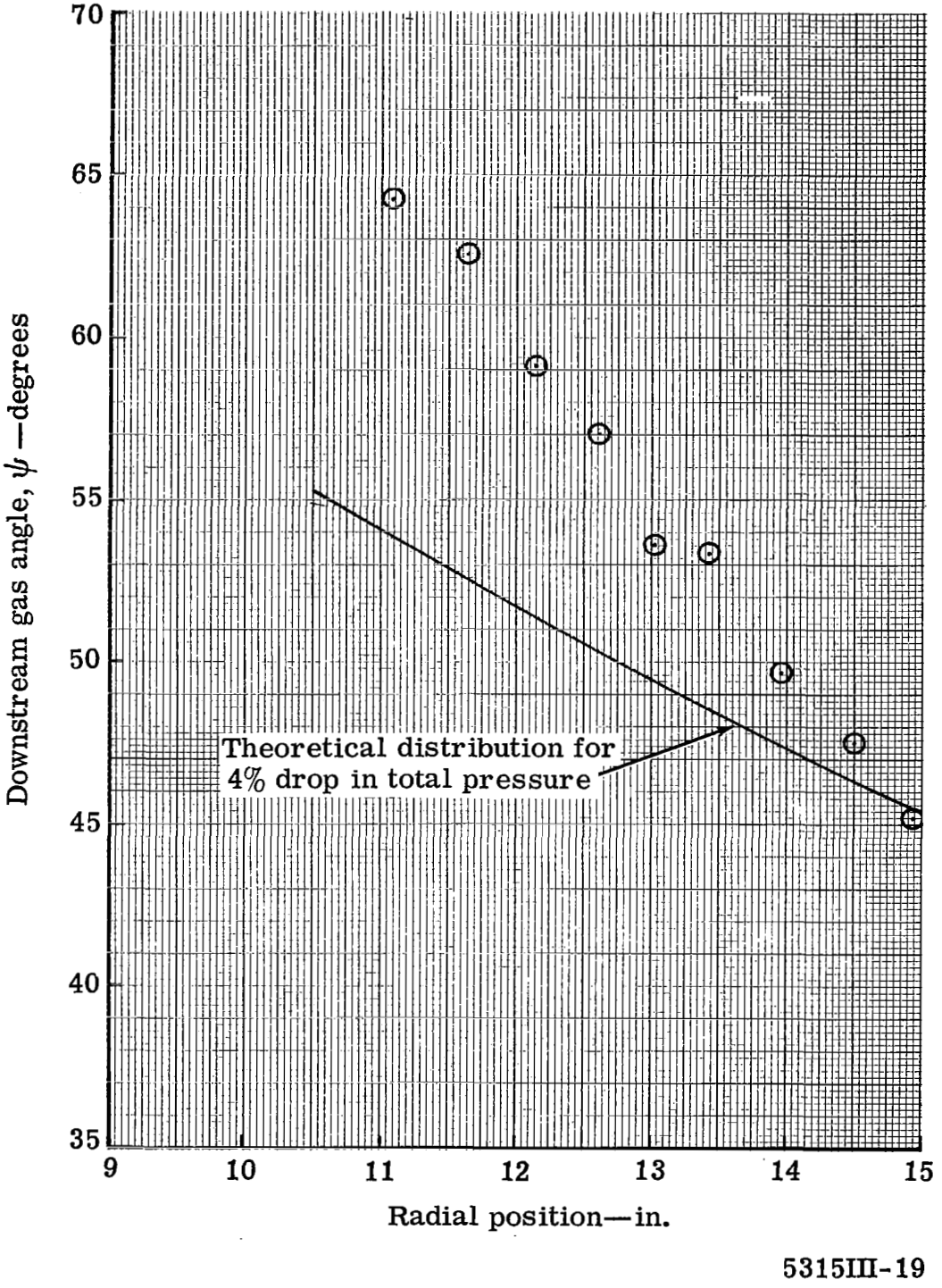

Figure 19. Measured and predicted radial variation of average downstream gas angle for tandem blade.

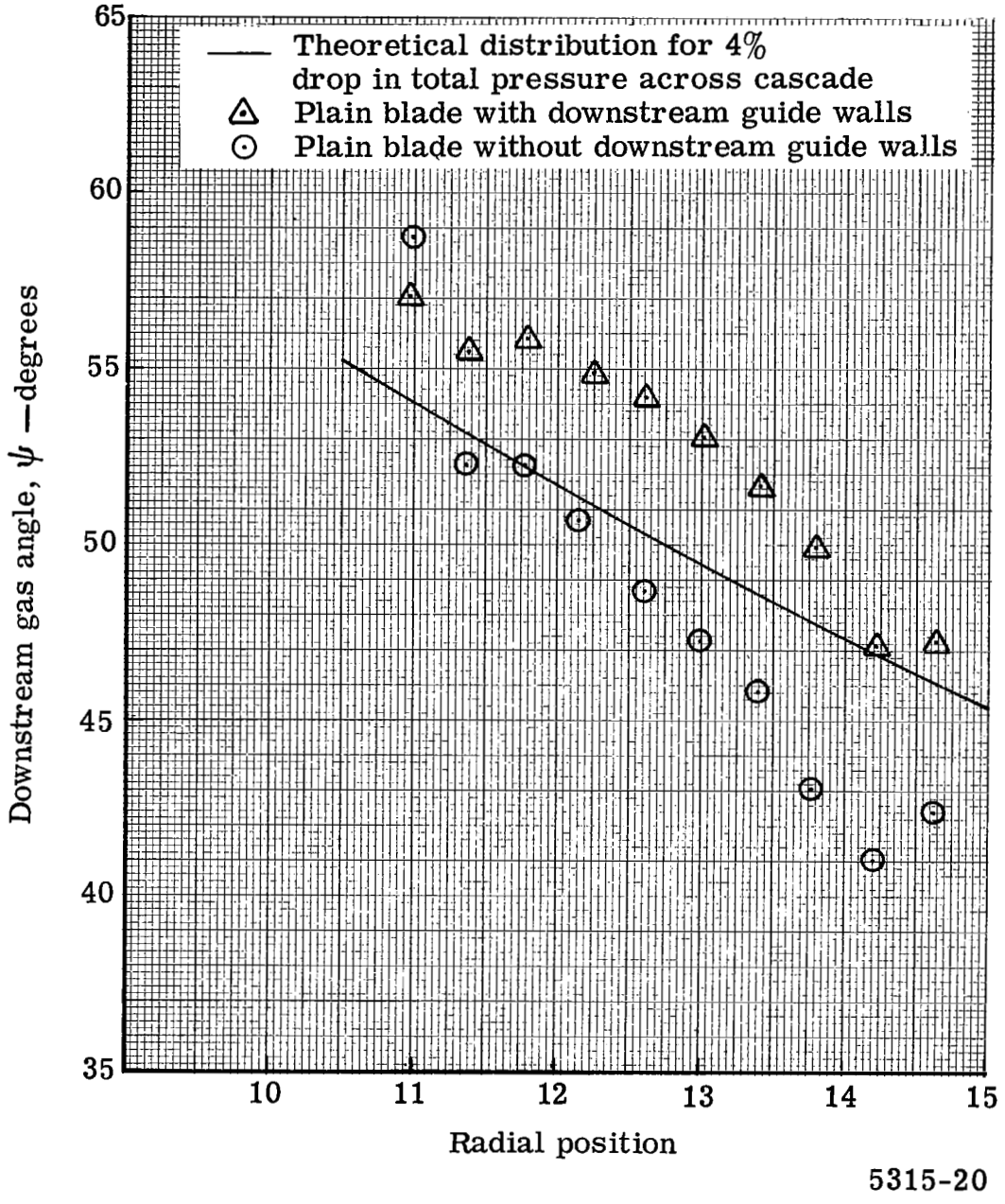

Figure 20. Measured and predicted radial variation of the plain blade average downstream gas angle.

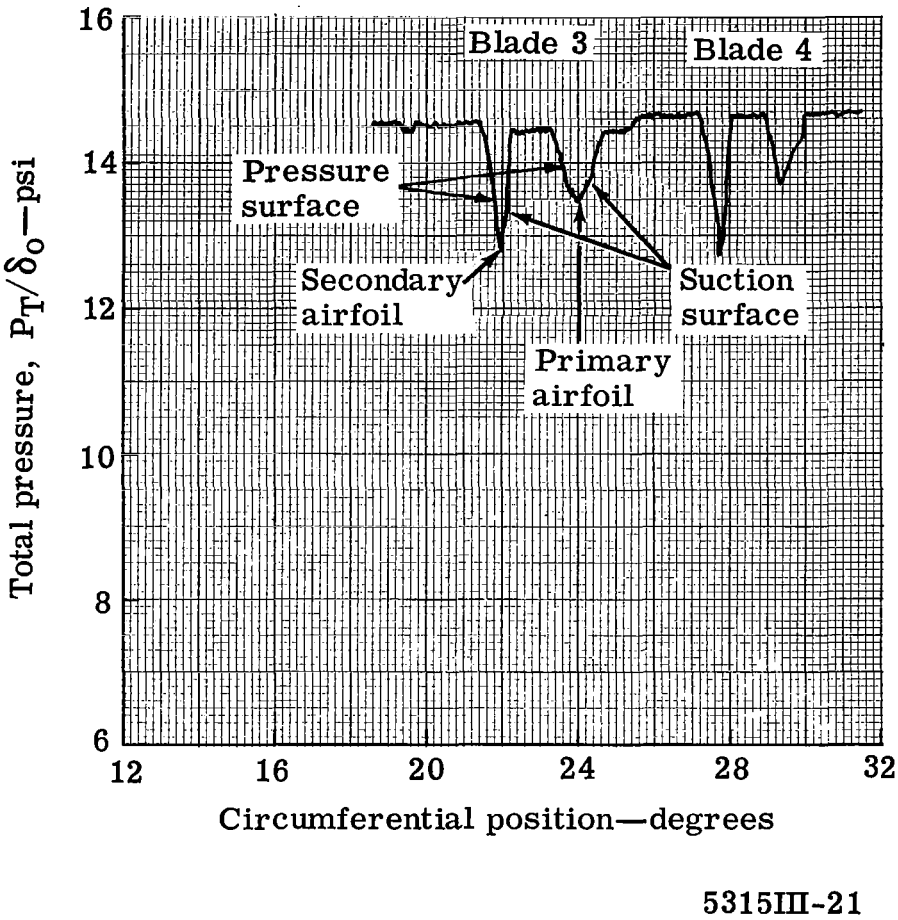

Figure 21. Tandem blade total pressure survey at station 3 for radial position, R = 13.01 in.

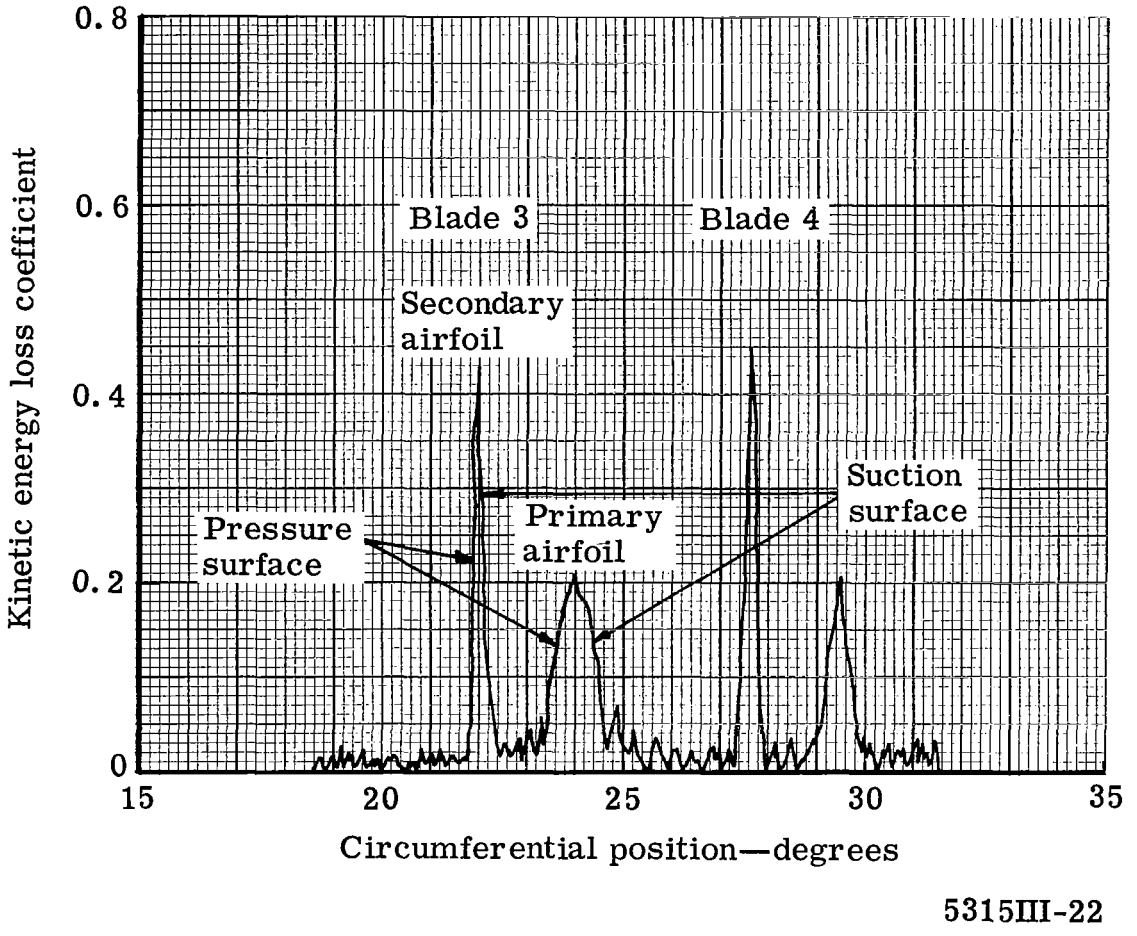

Figure 22. Tandem blade kinetic energy loss circumferential distribution at station 3 for radial position, R = 13.01 in.

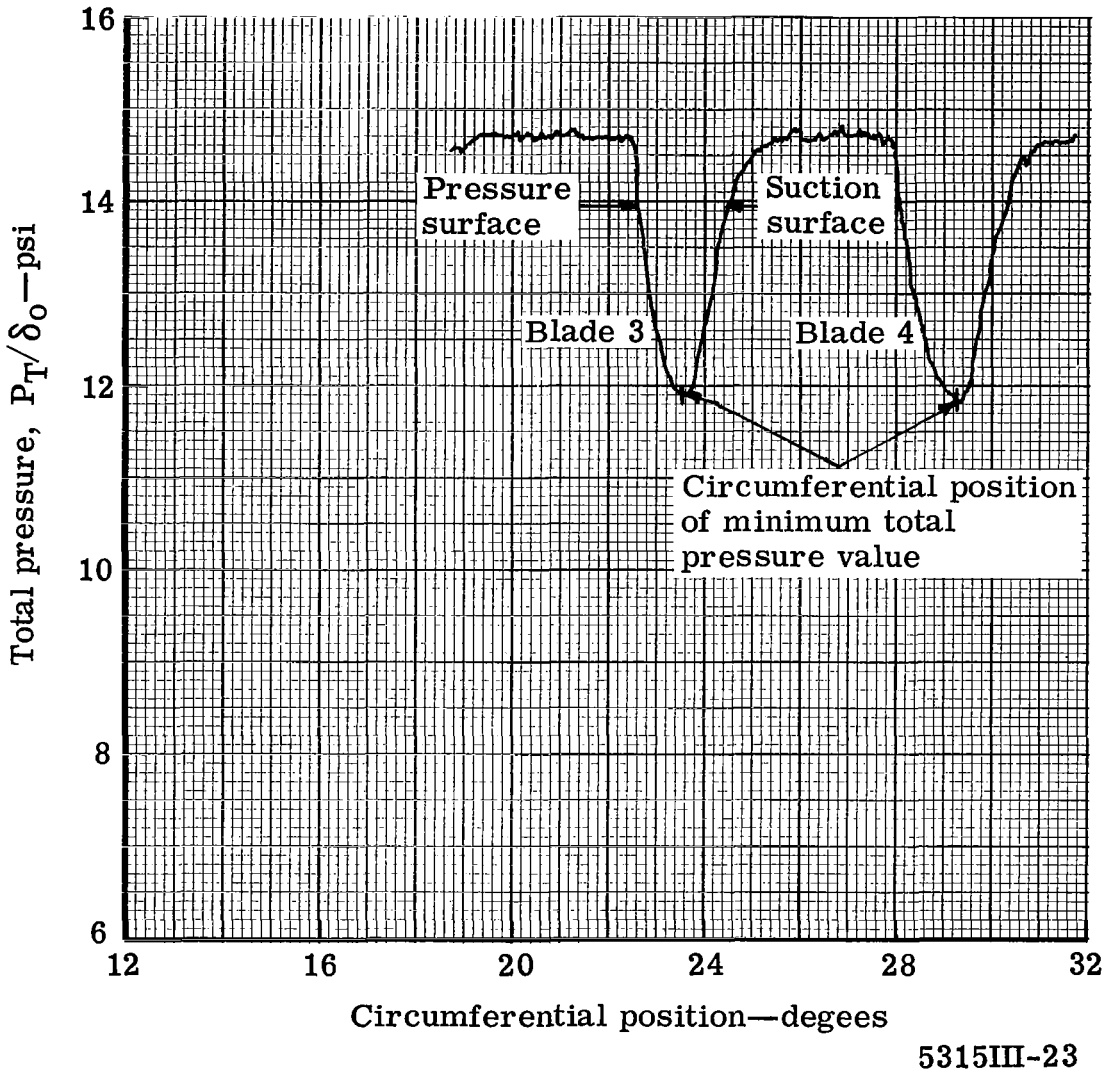

Figure 23. Plain blade exit wake survey total pressure distribution for radial position, R = 12.97 in.

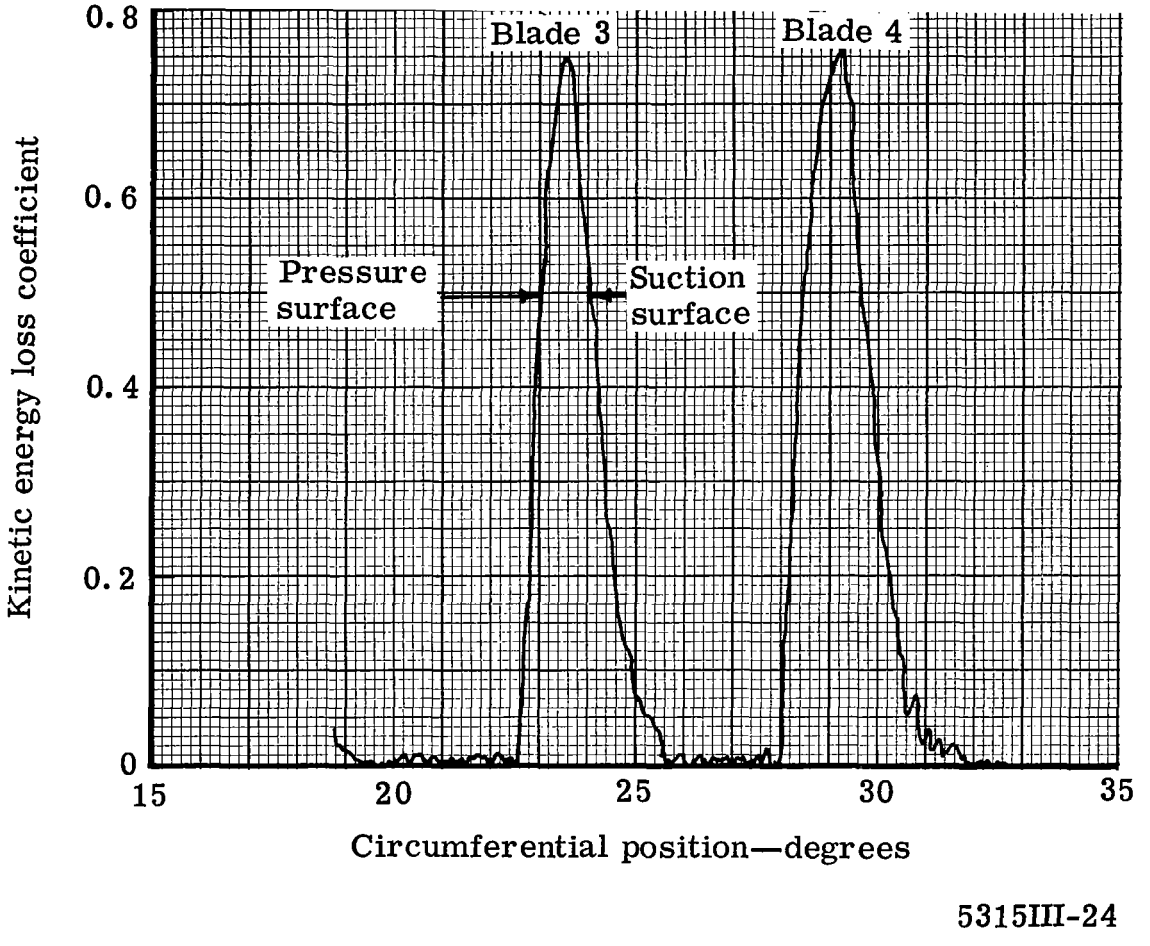

Figure 24. Plain blade circumferential variation of station 3 kinetic energy loss coefficient for radial position, R = 12.97 in.

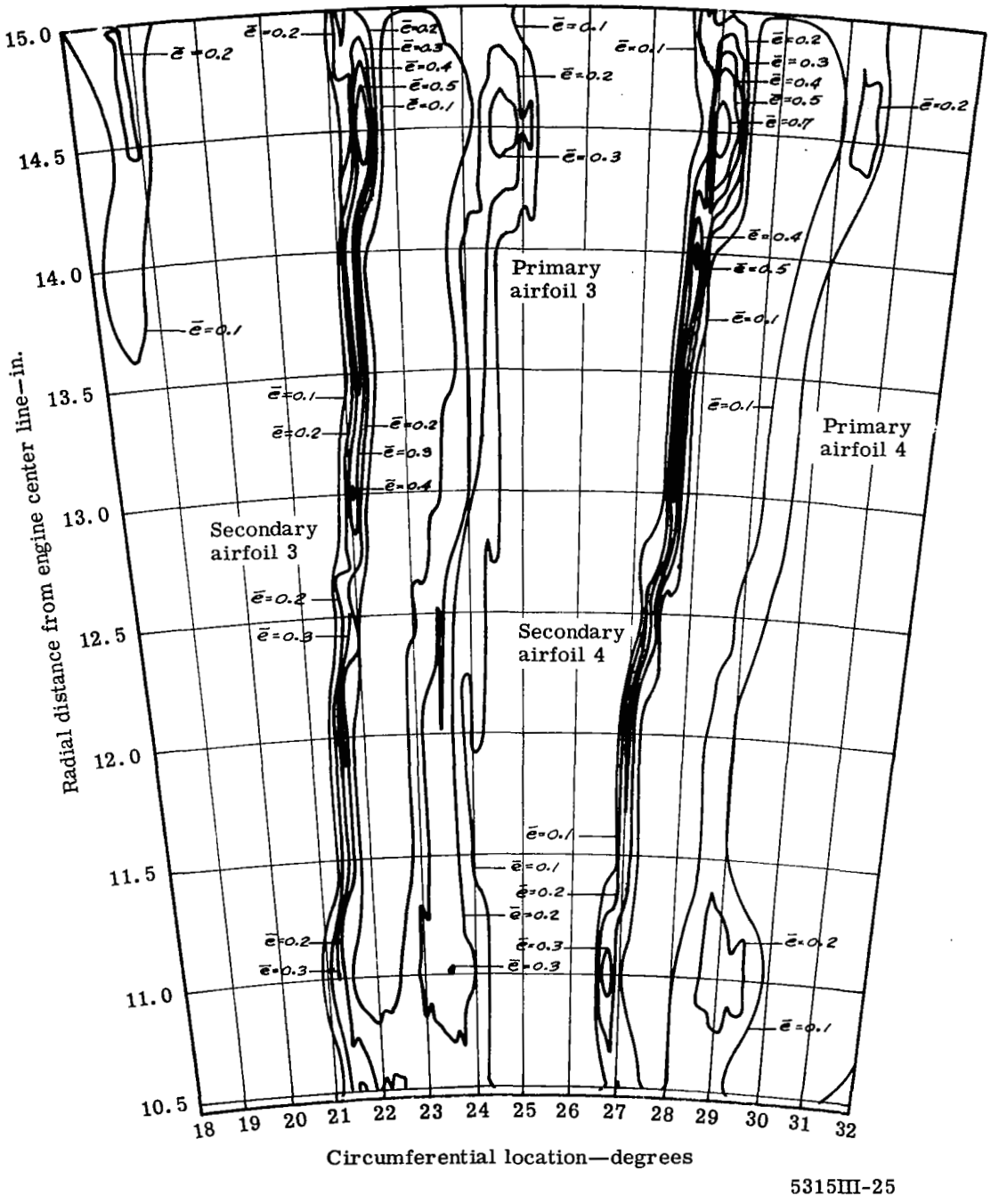

Figure 25. Contours of kinetic energy loss coefficient across one tandem blade passage at station 3.

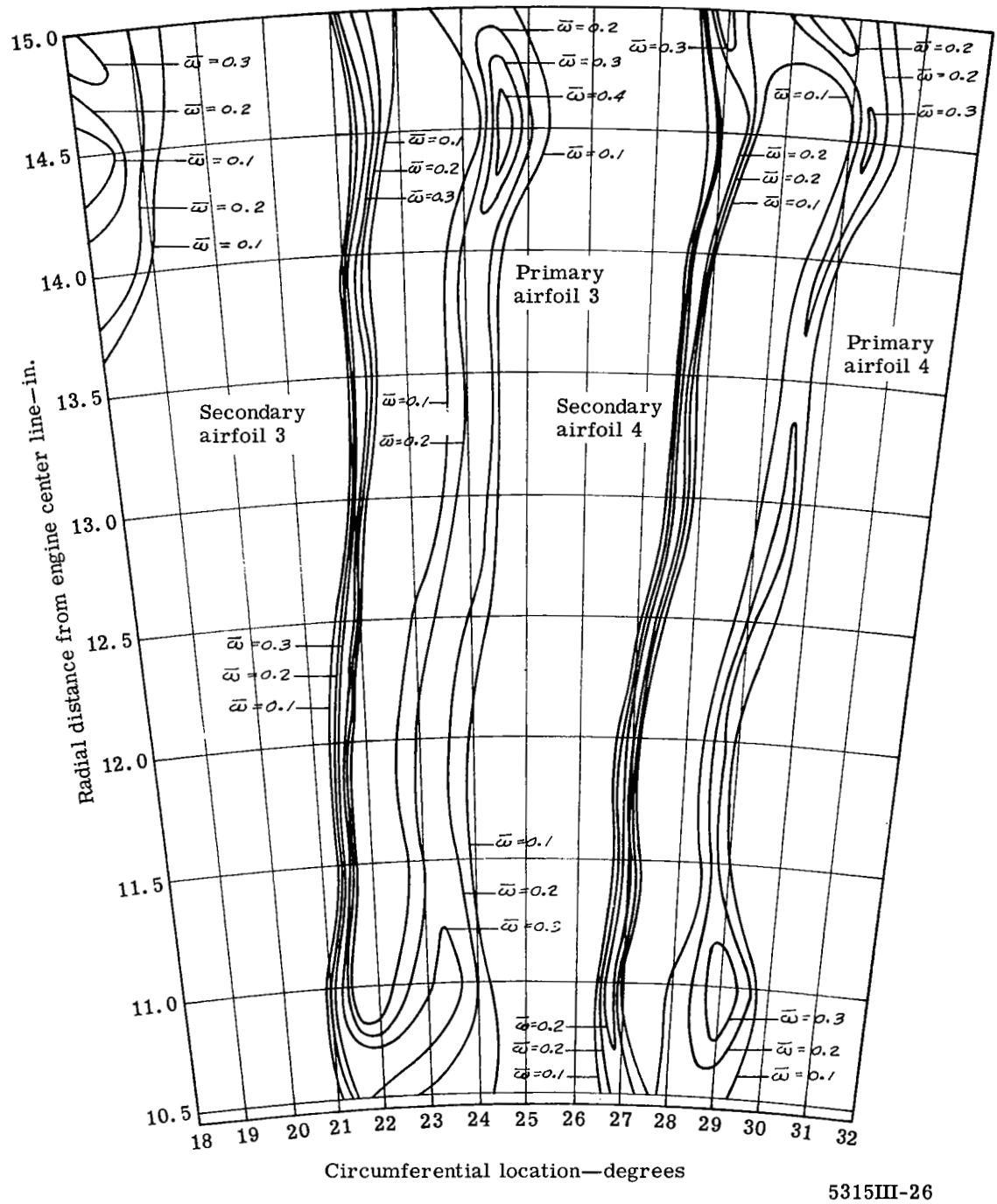

Figure 26. Contours of total pressure loss coefficient across one tandem blade passage at station 3.

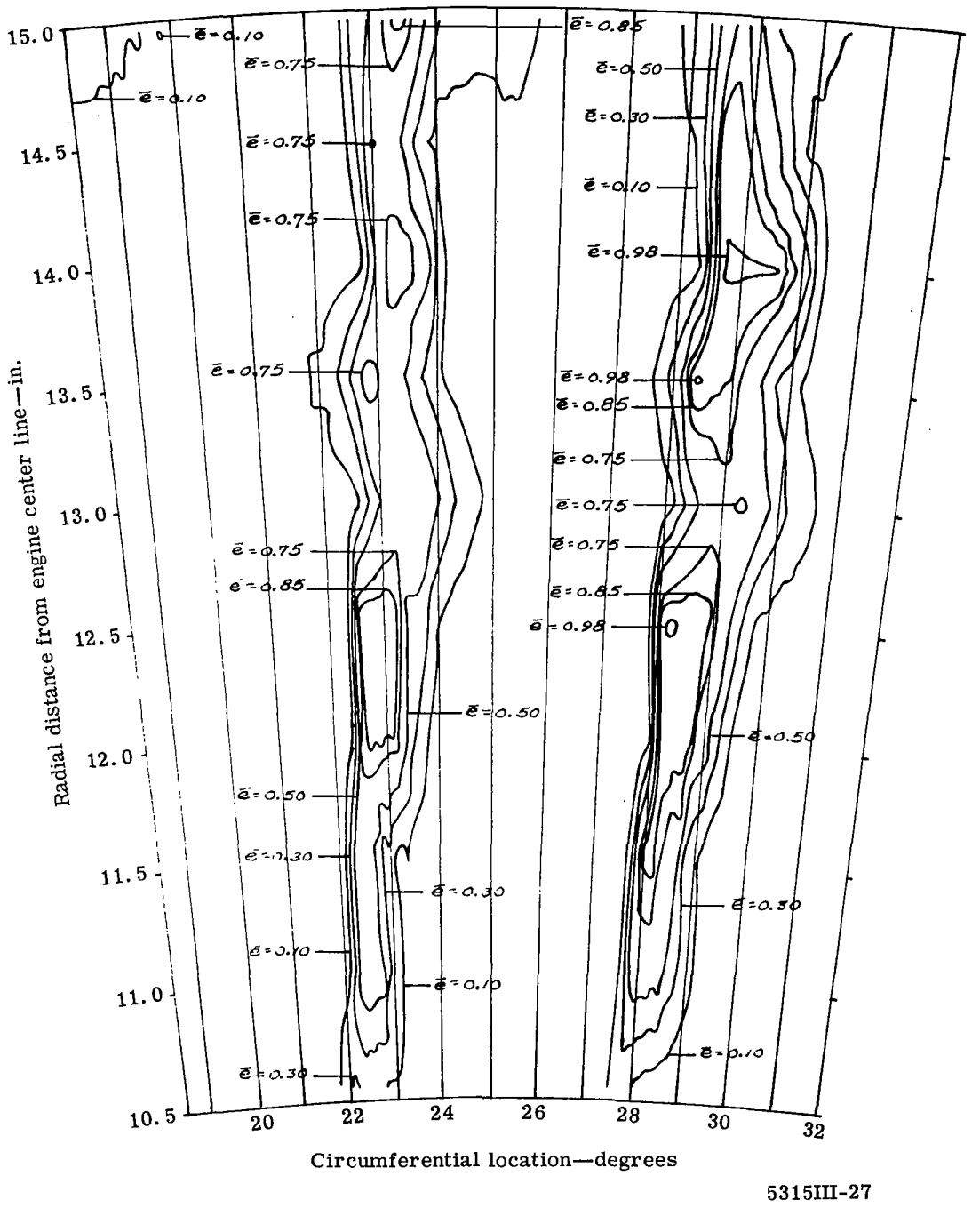

Figure 27. Contours of kinetic energy loss coefficient across one plain blade passage at station 3.

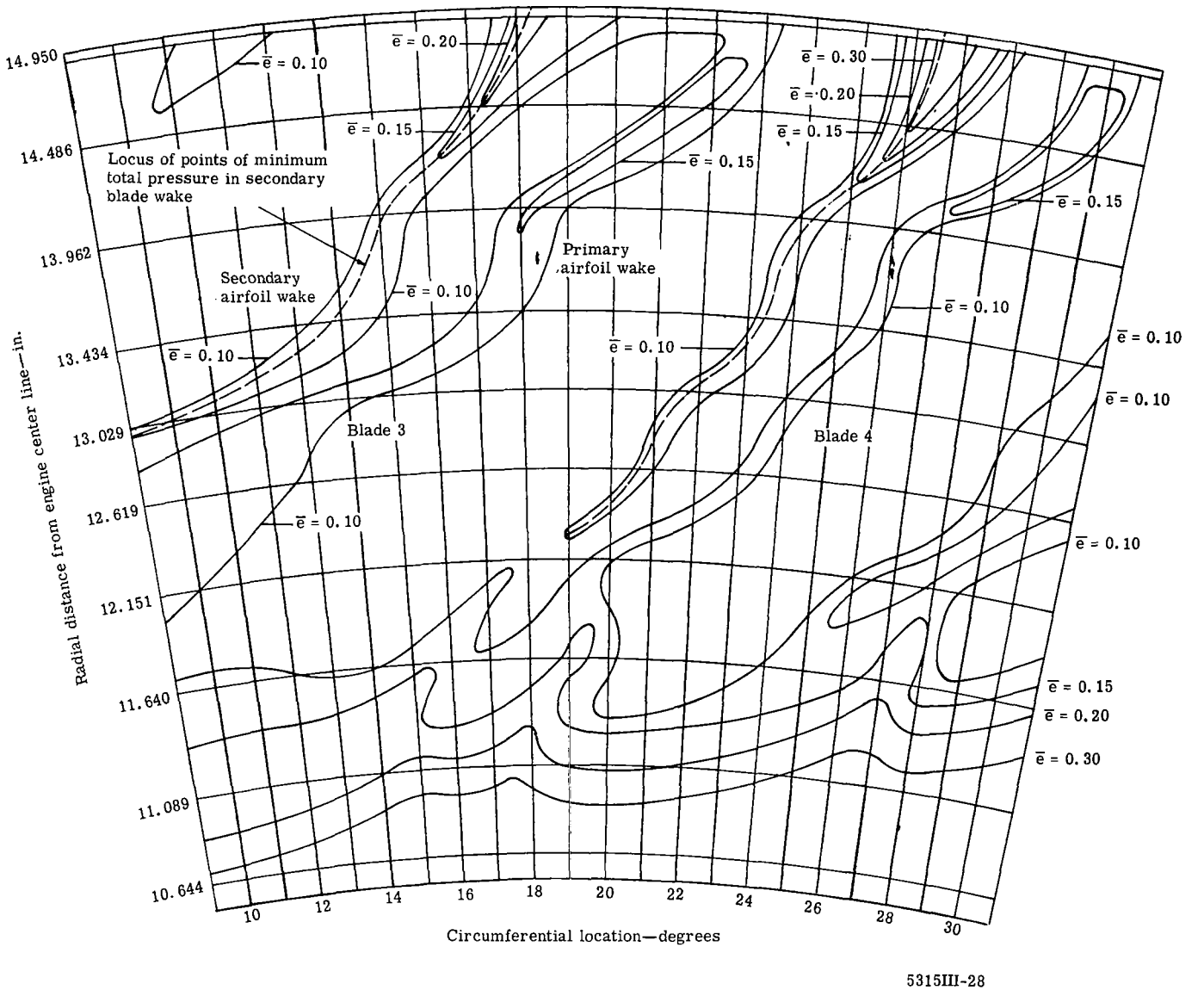

Figure 28. Contours of kinetic energy loss coefficient at station 4 for the tandem blade.

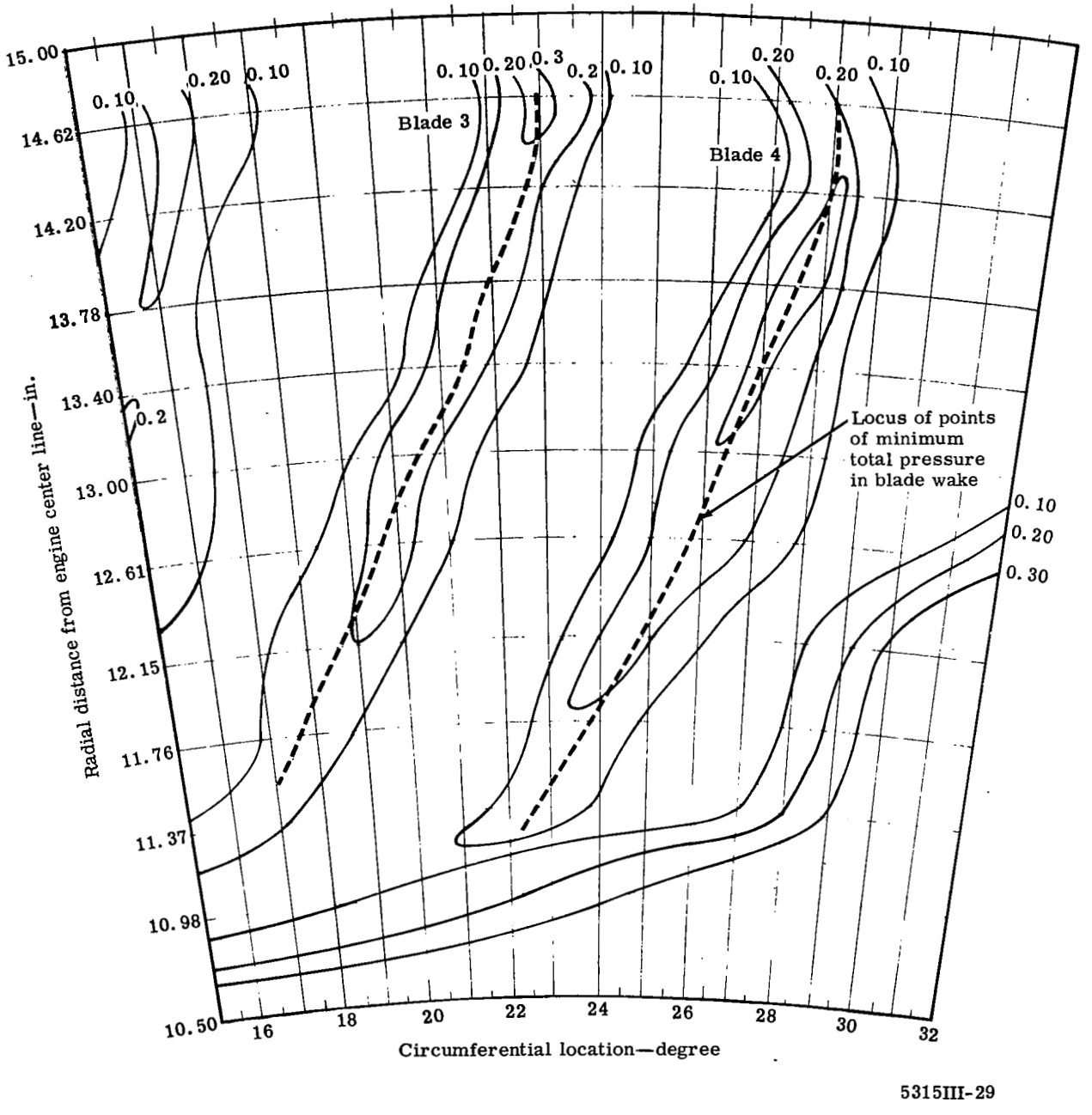

Figure 29. Contours of kinetic energy loss coefficient at station 4 for the plain blade.

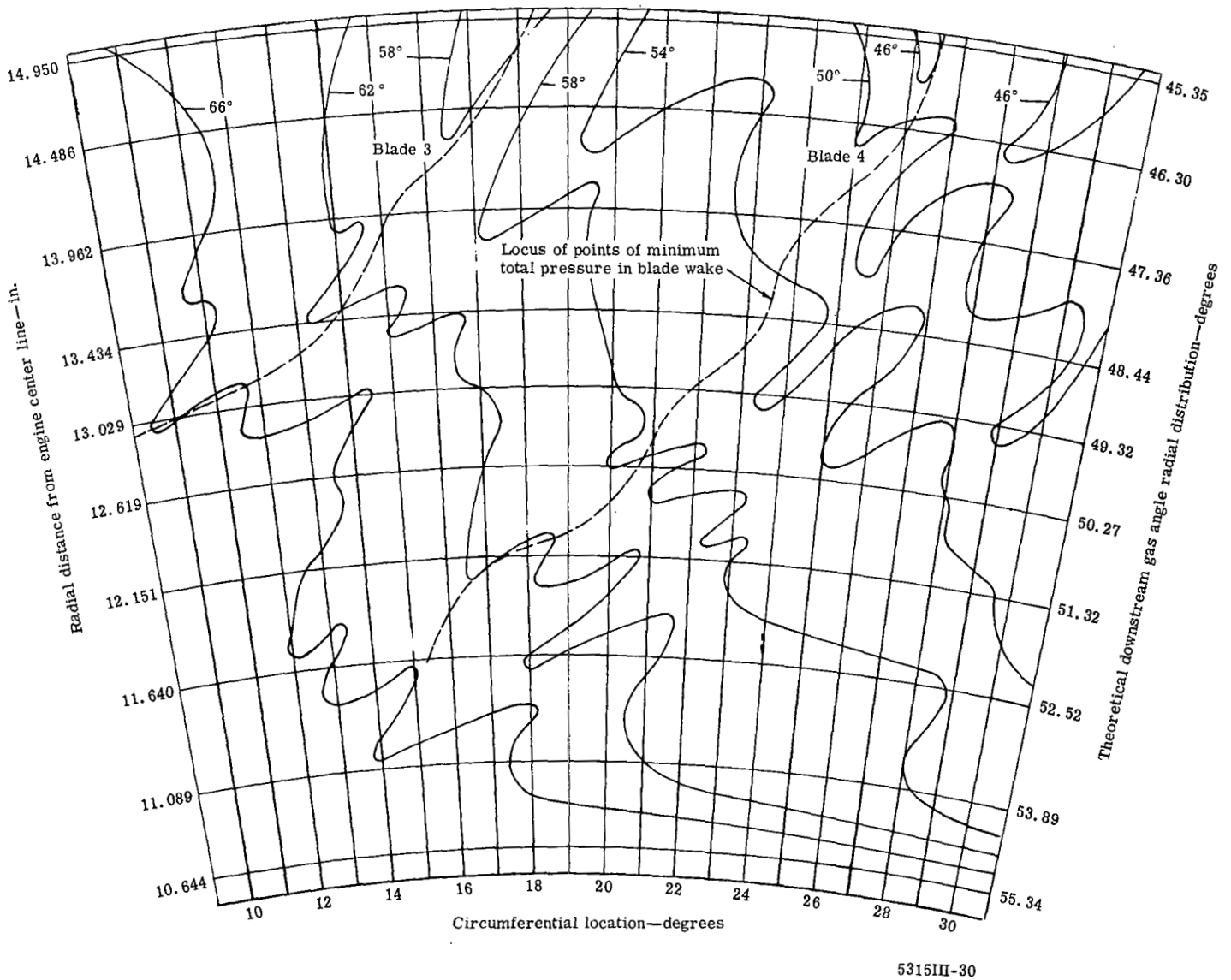

Figure 30. Contours of downstream gas angle—measured from axial—for the tandem blade at station 4.

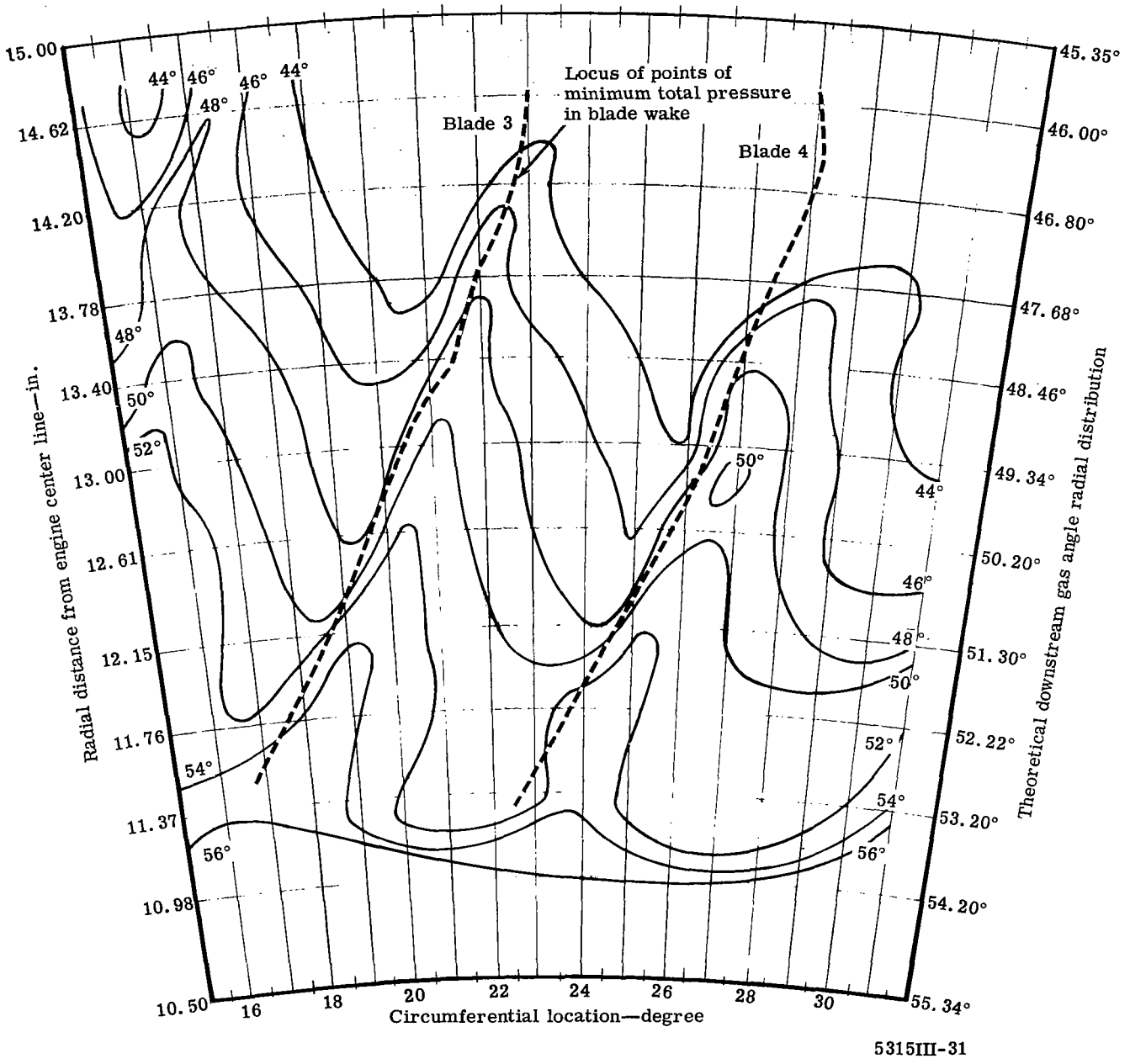

Figure 31. Contours of downstream gas angle—measured from axial—for the plain blade at station 4.

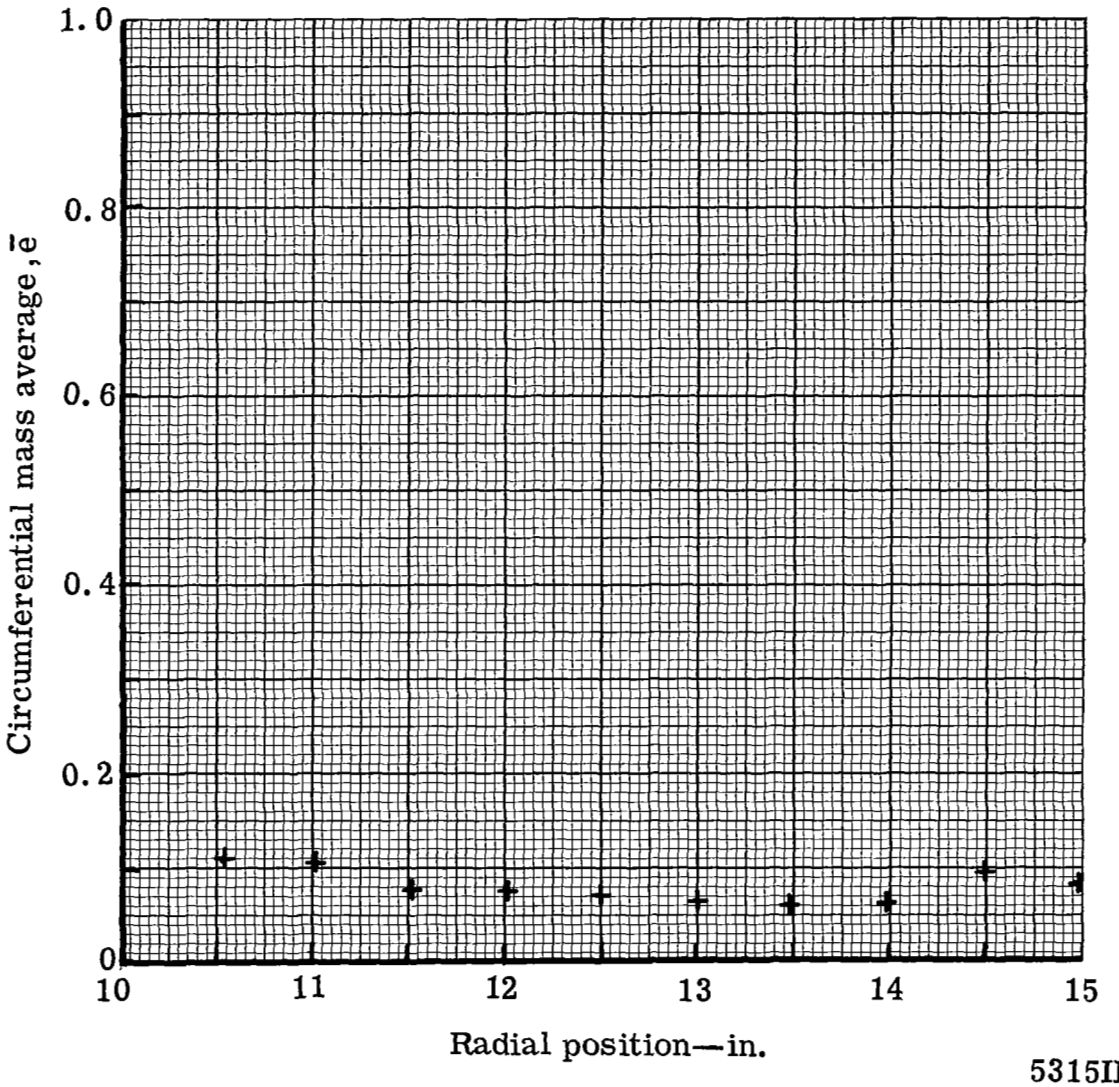

Figure 32. Tandem blade exit wake survey-kinetic energy loss coefficient distribution at station 3.

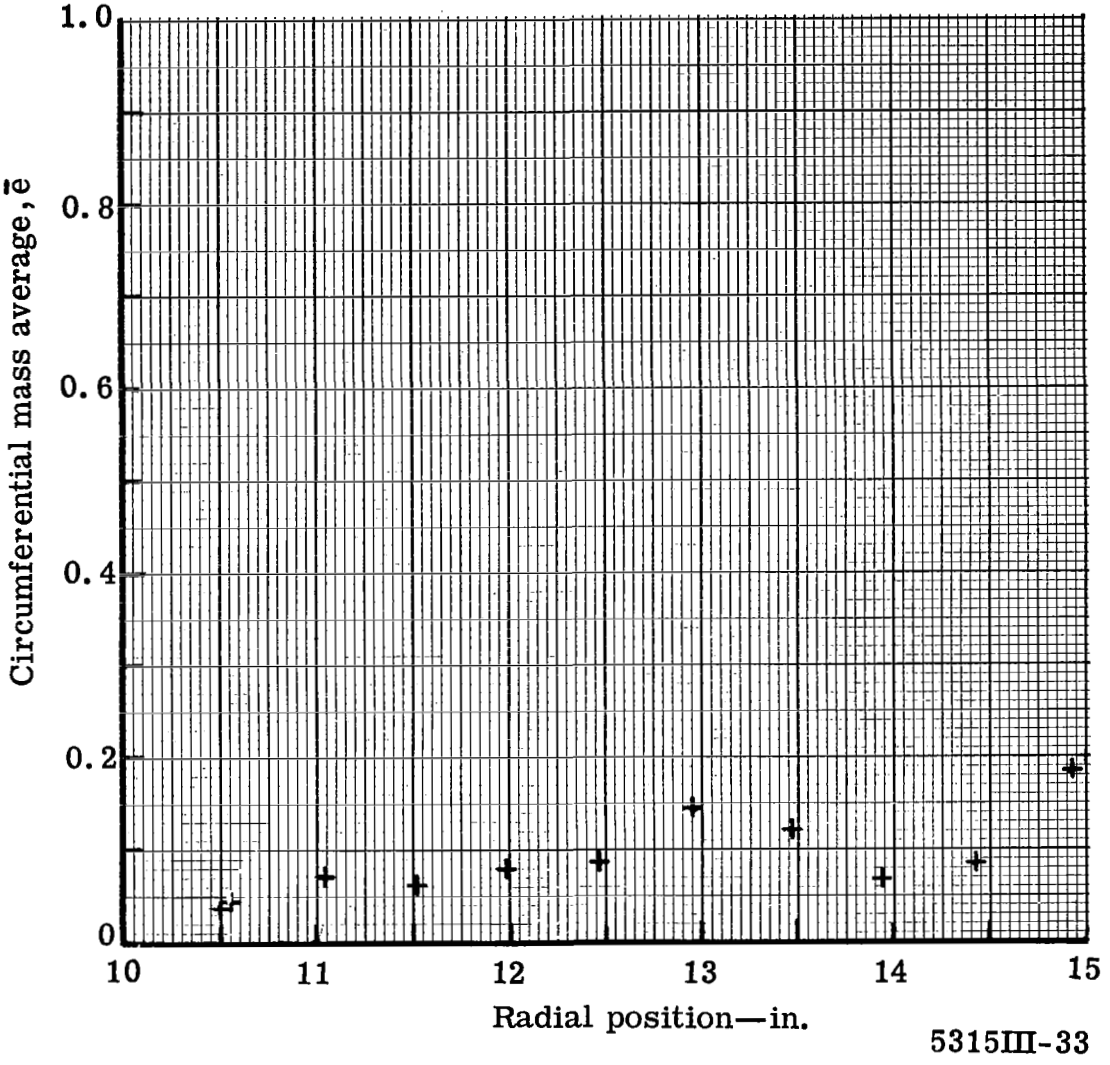

Figure 33. Plain blade exit wake survey-kinetic energy loss coefficient distribution at station 3.

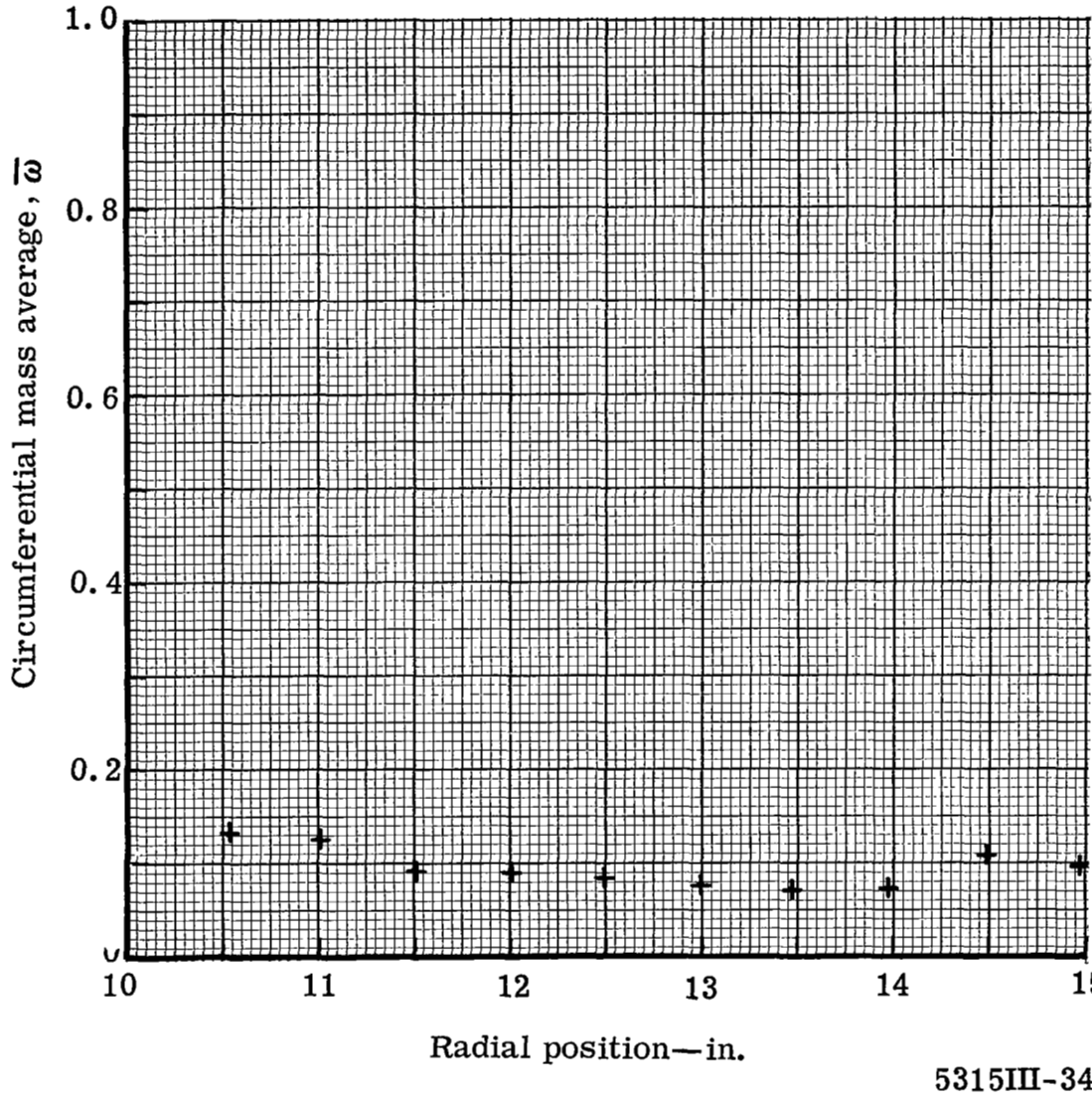

Figure 34. Tandem blade exit wake survey-total pressure loss coefficient distribution at station 3.

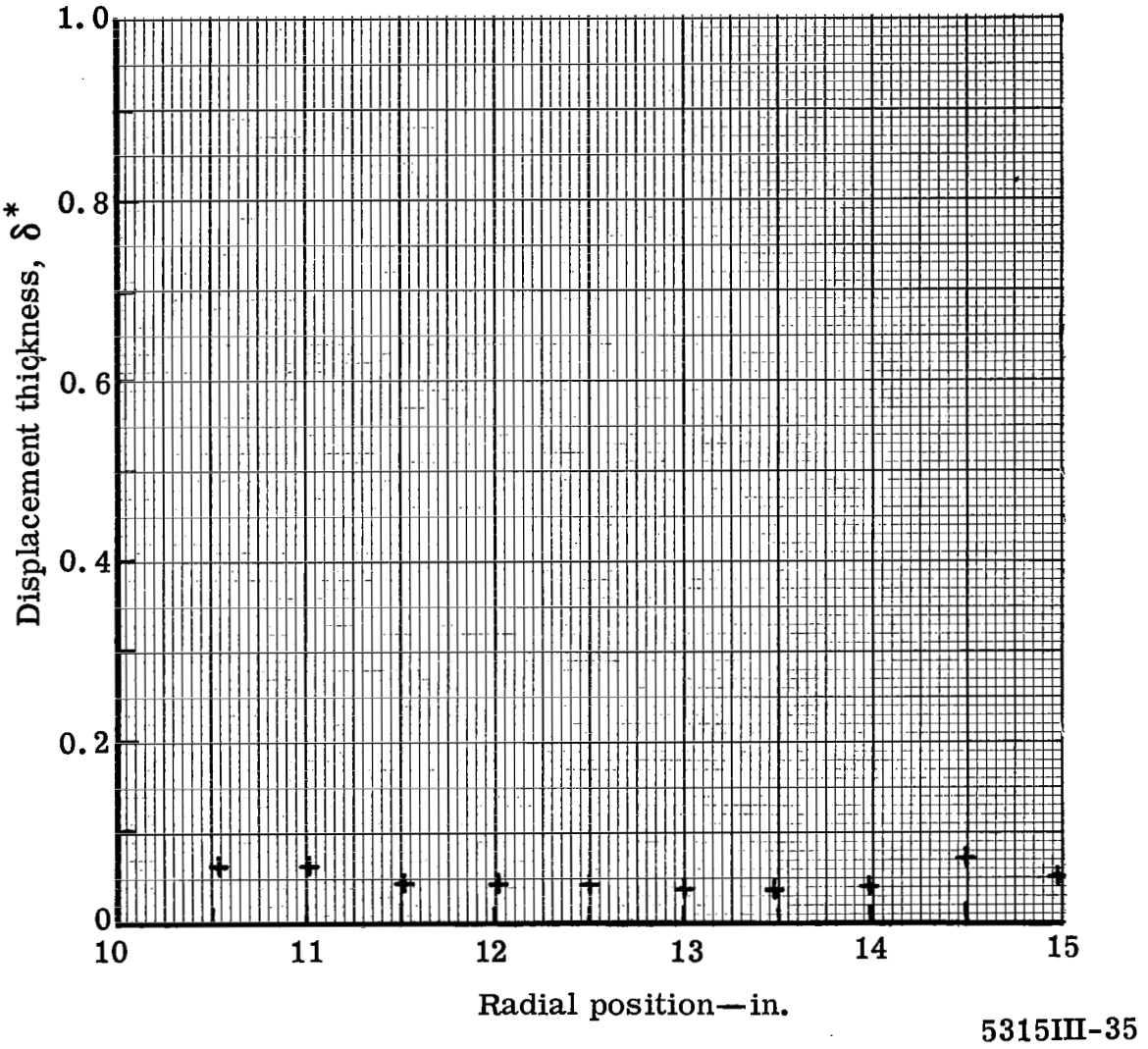

Figure 35. Tandem blade exit wake survey-displacement thickness distribution at station 3.

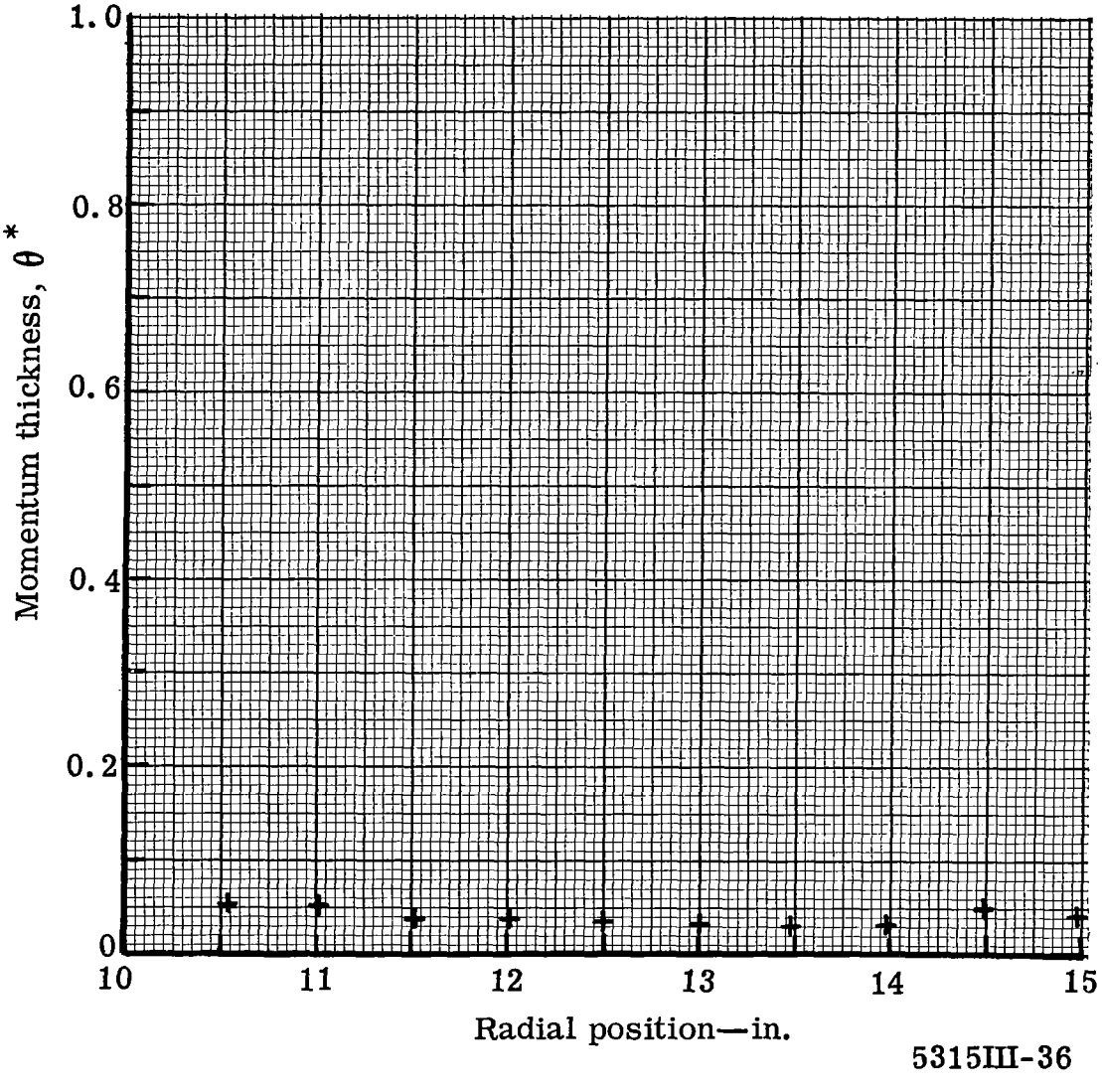

Figure 36. Tandem blade exit wake survey-momentum thickness distribution at station 3.

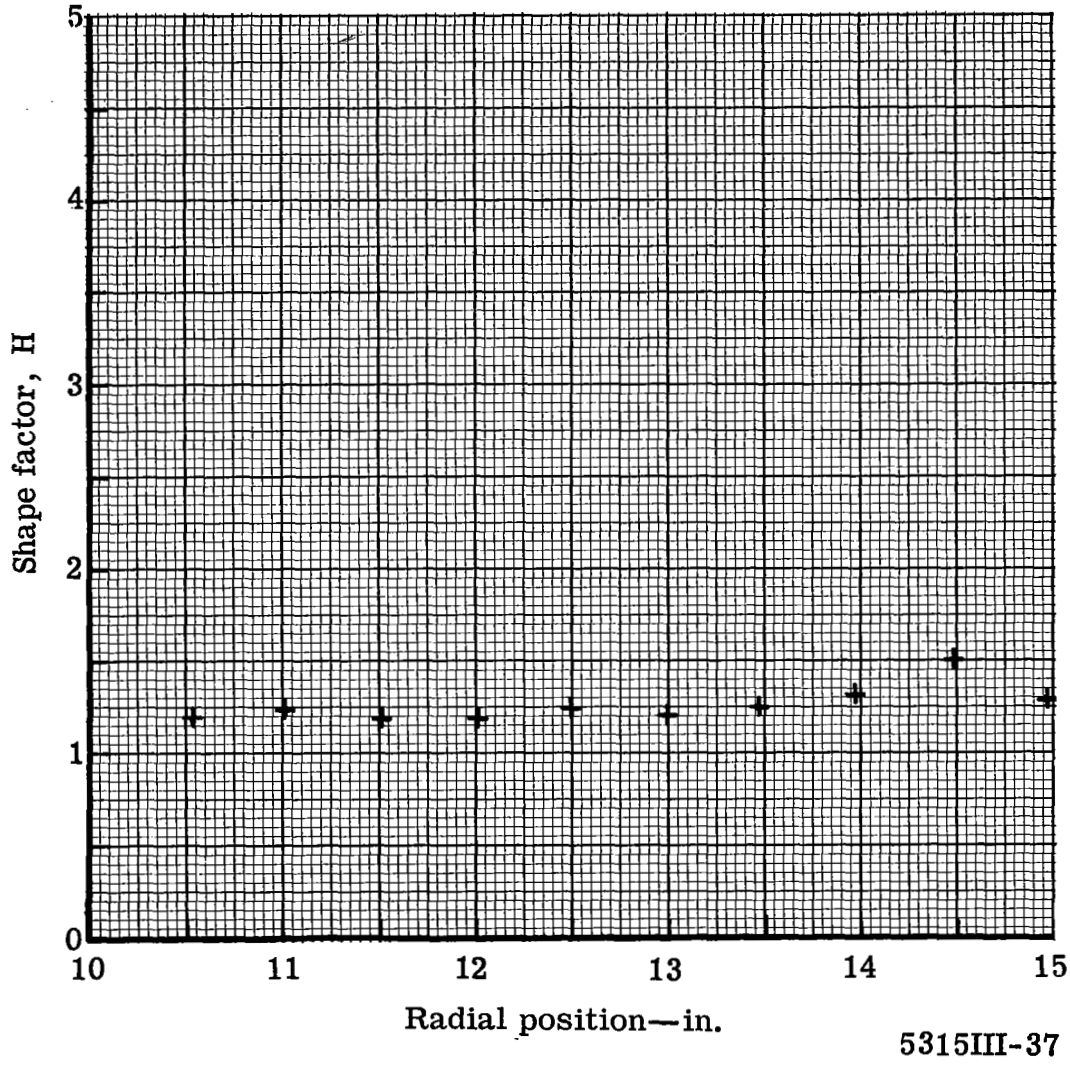

Figure 37. Tandem blade exit wake survey-shape factor distribution at station 3.

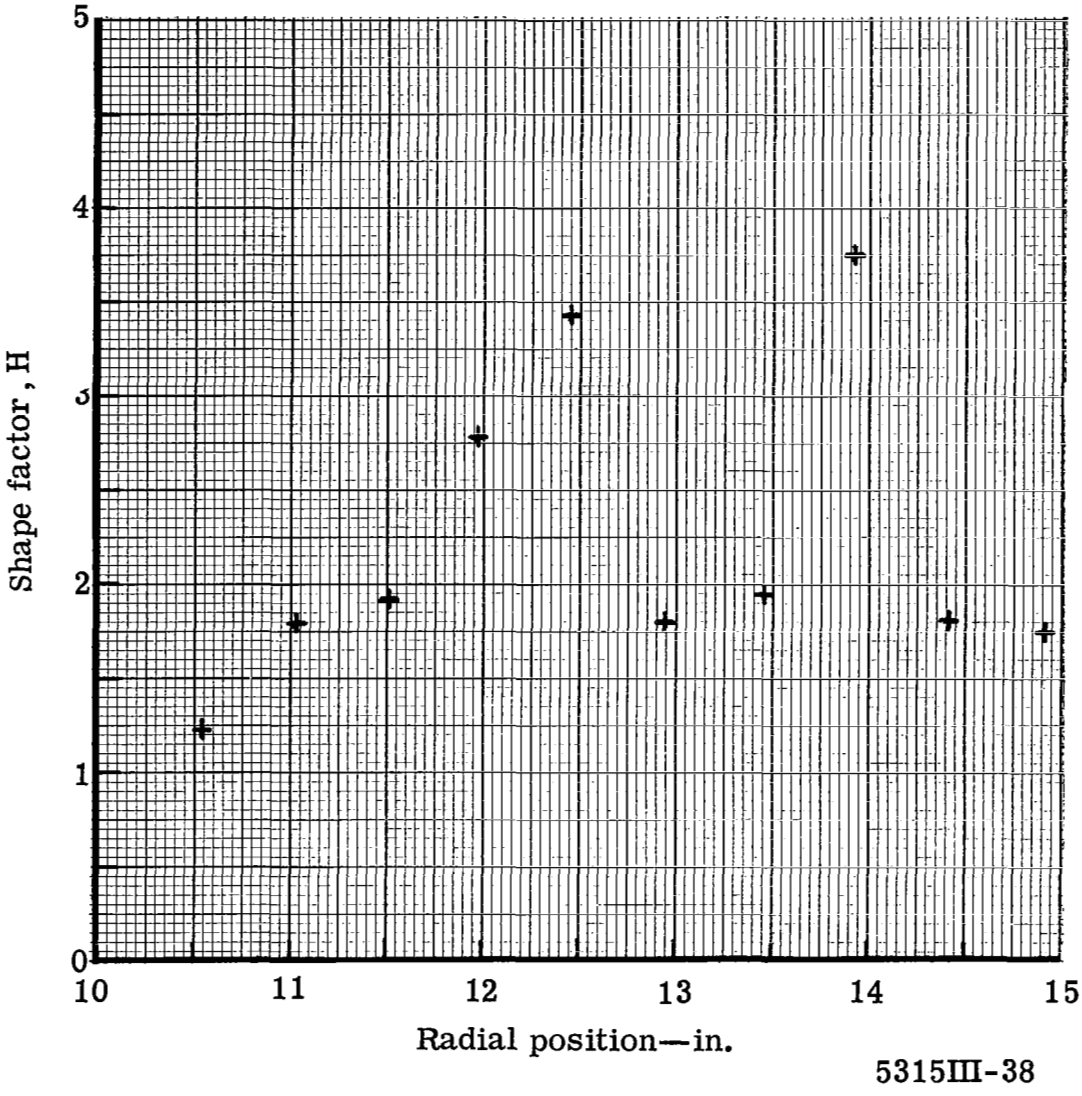

Figure 38. Plain blade exit wake survey-shape factor distribution at station 3.

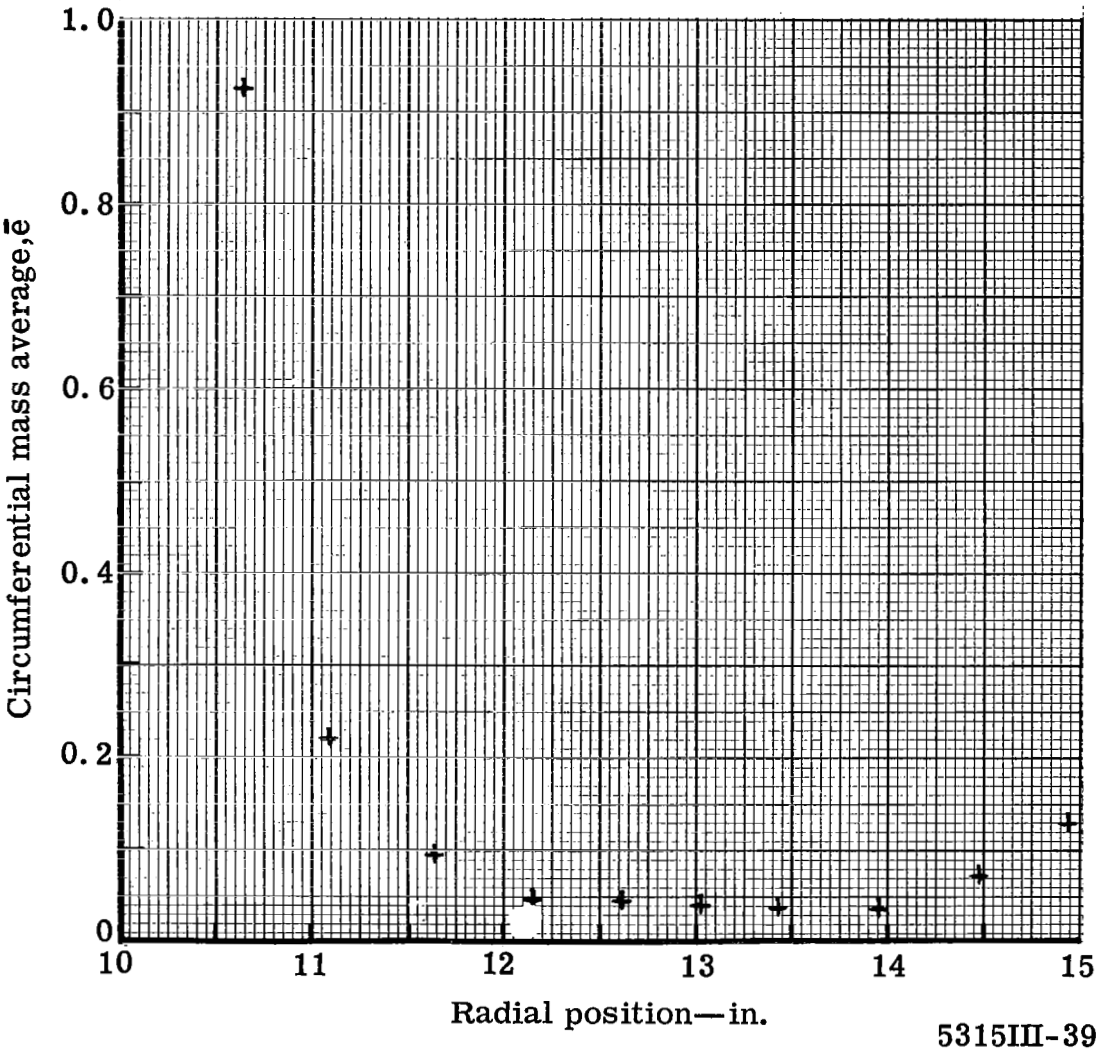

Figure 39. Tandem blade downstream wake survey-kinetic energy loss coefficient distribution at station 4.

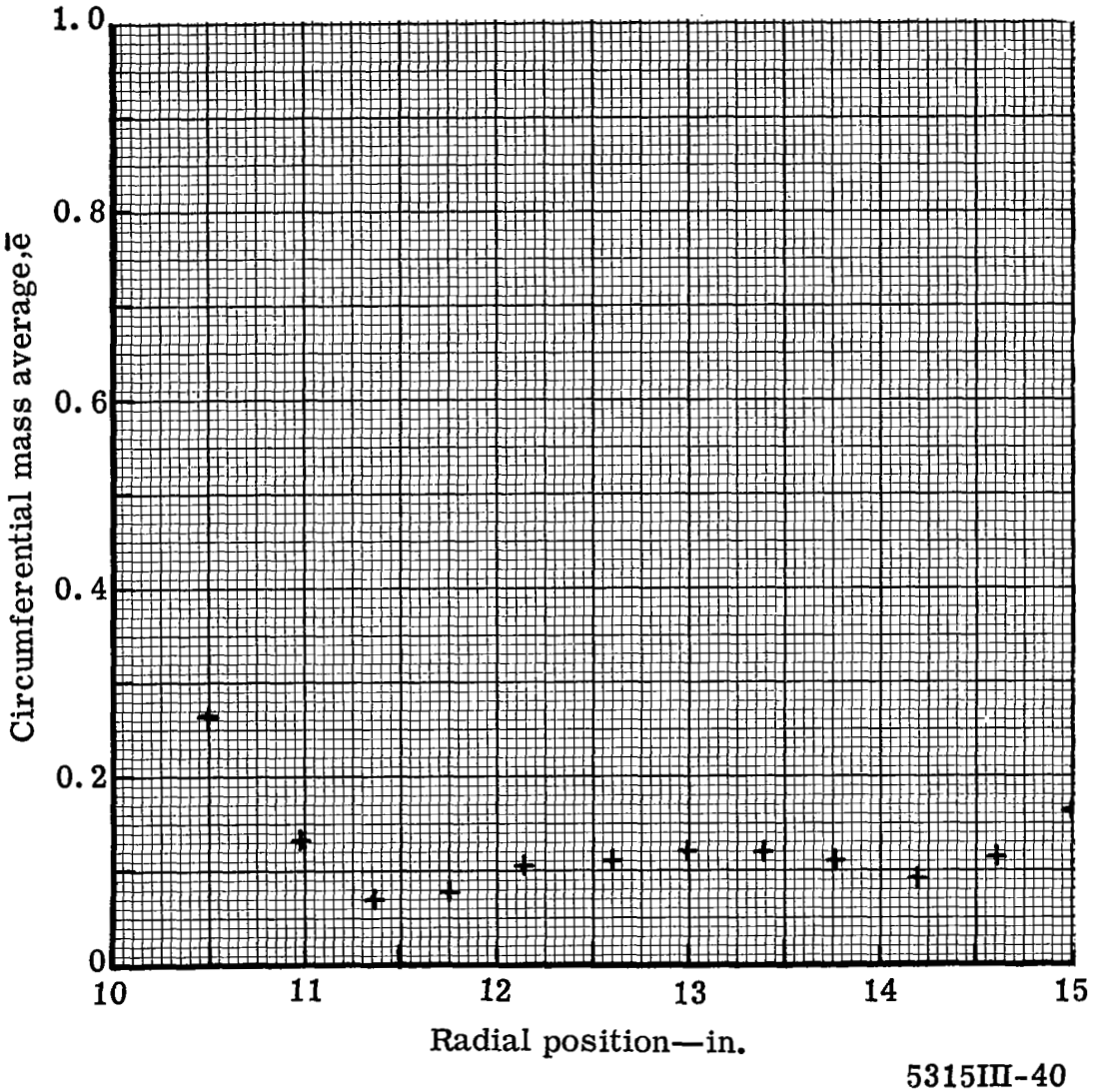

Figure 40. Plain blade downstream wake survey-kinetic energy loss coefficient distribution at station 4.

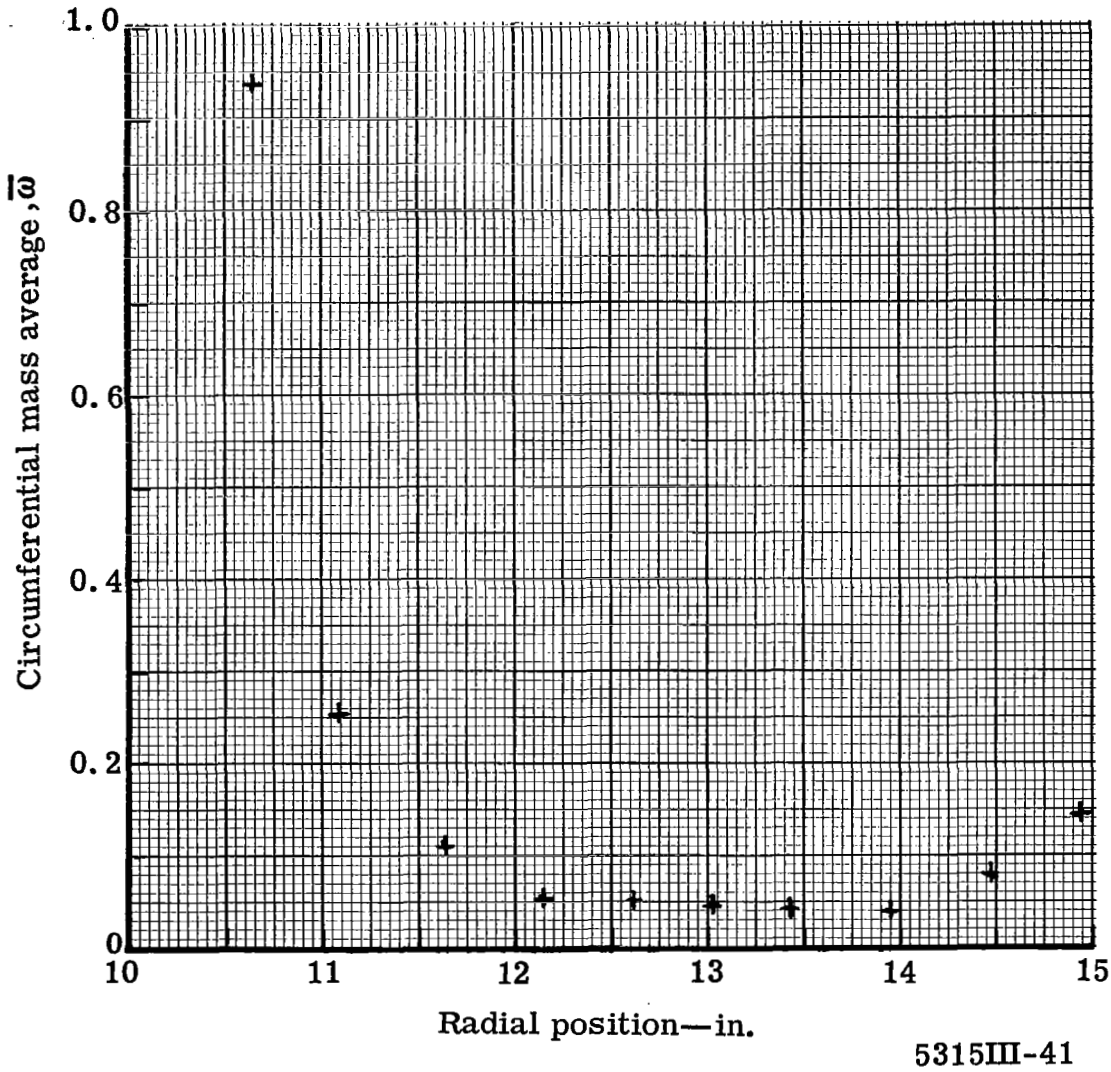

Figure 41. Tandem blade downstream wake survey-total pressure loss coefficient distribution at station 4.

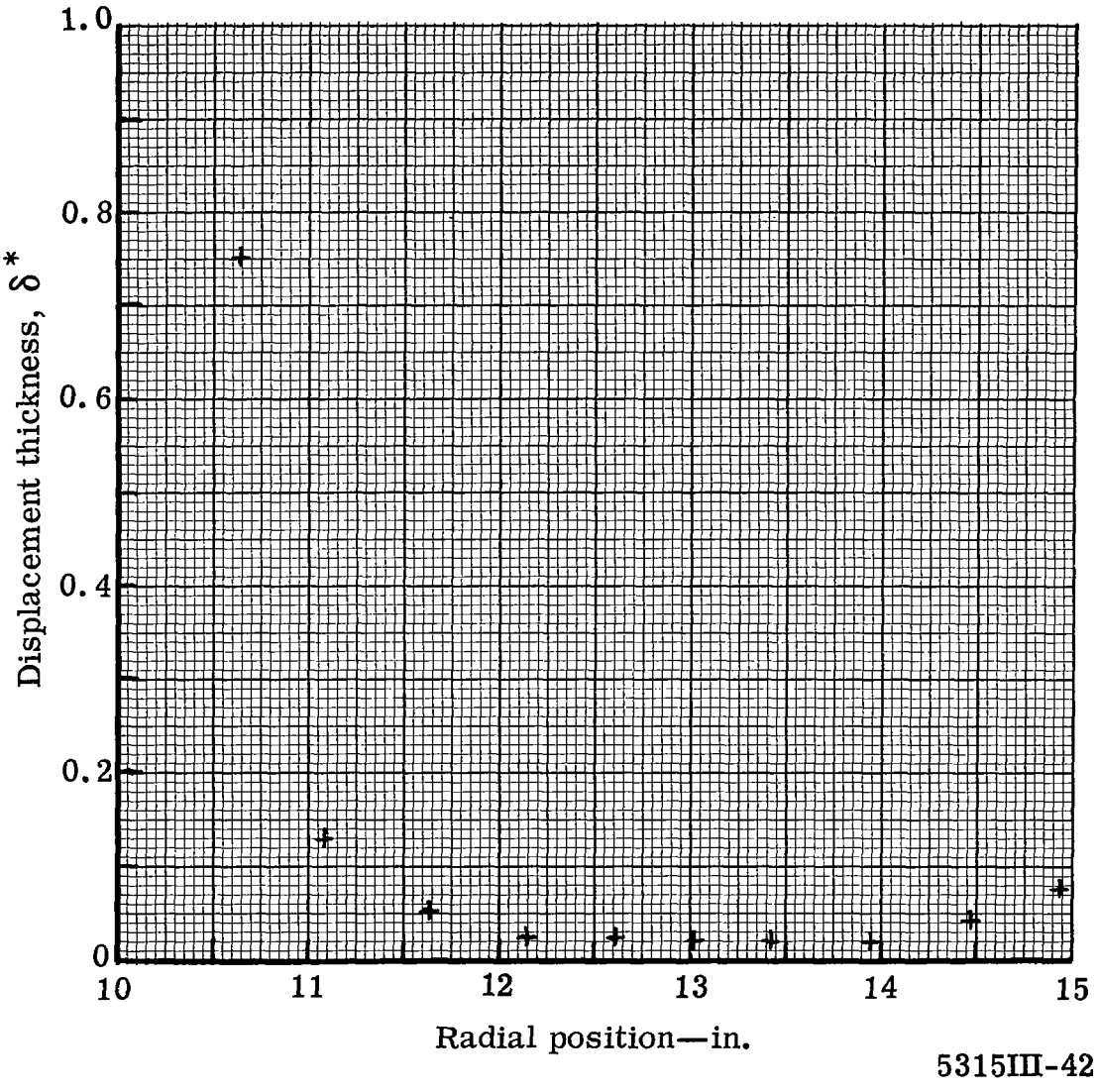

Figure 42. Tandem blade downstream wake survey-displacement thickness distribution at station 4.

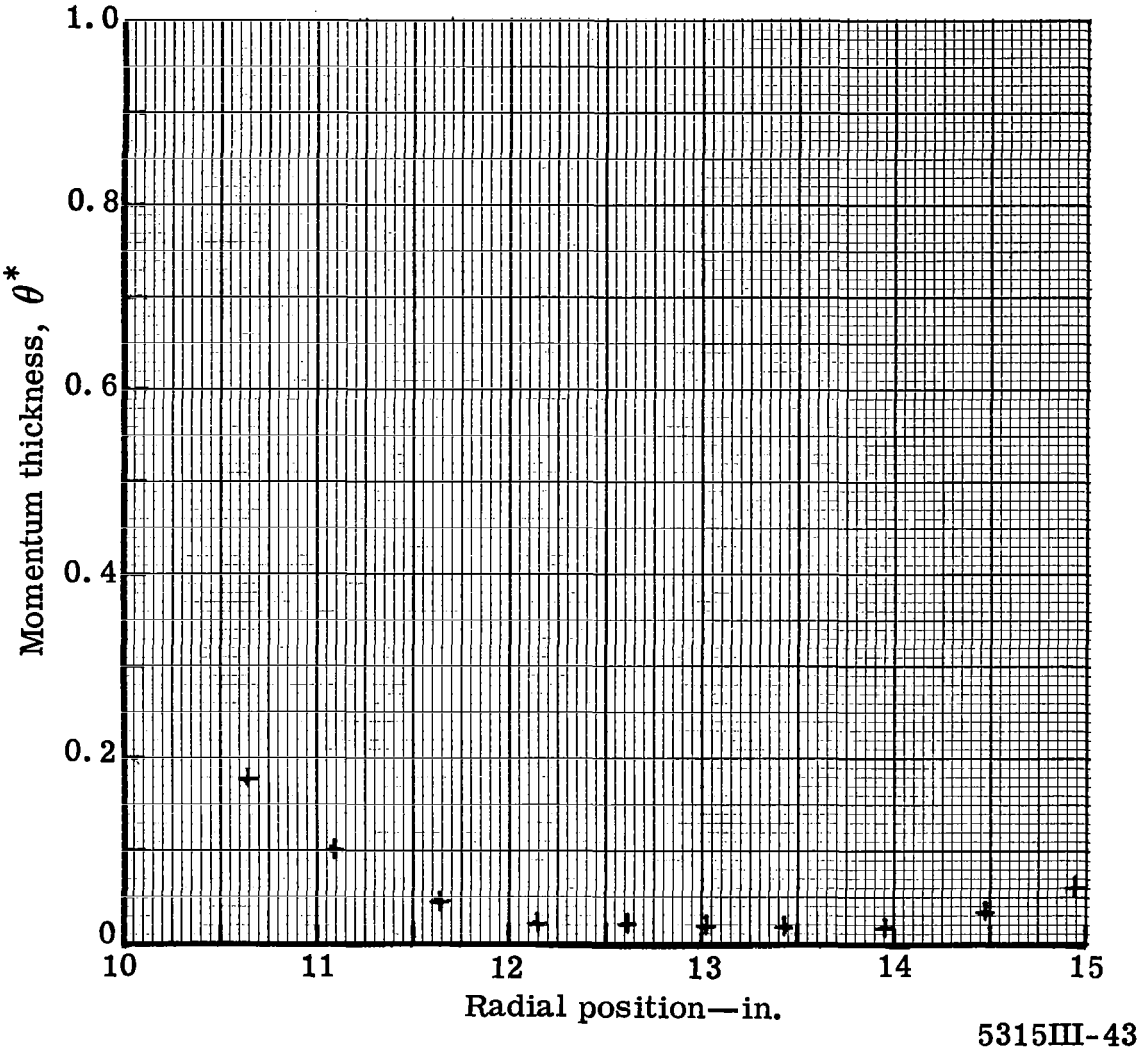

Figure 43. Tandem blade downstream wake survey-momentum thickness distribution at station 4.

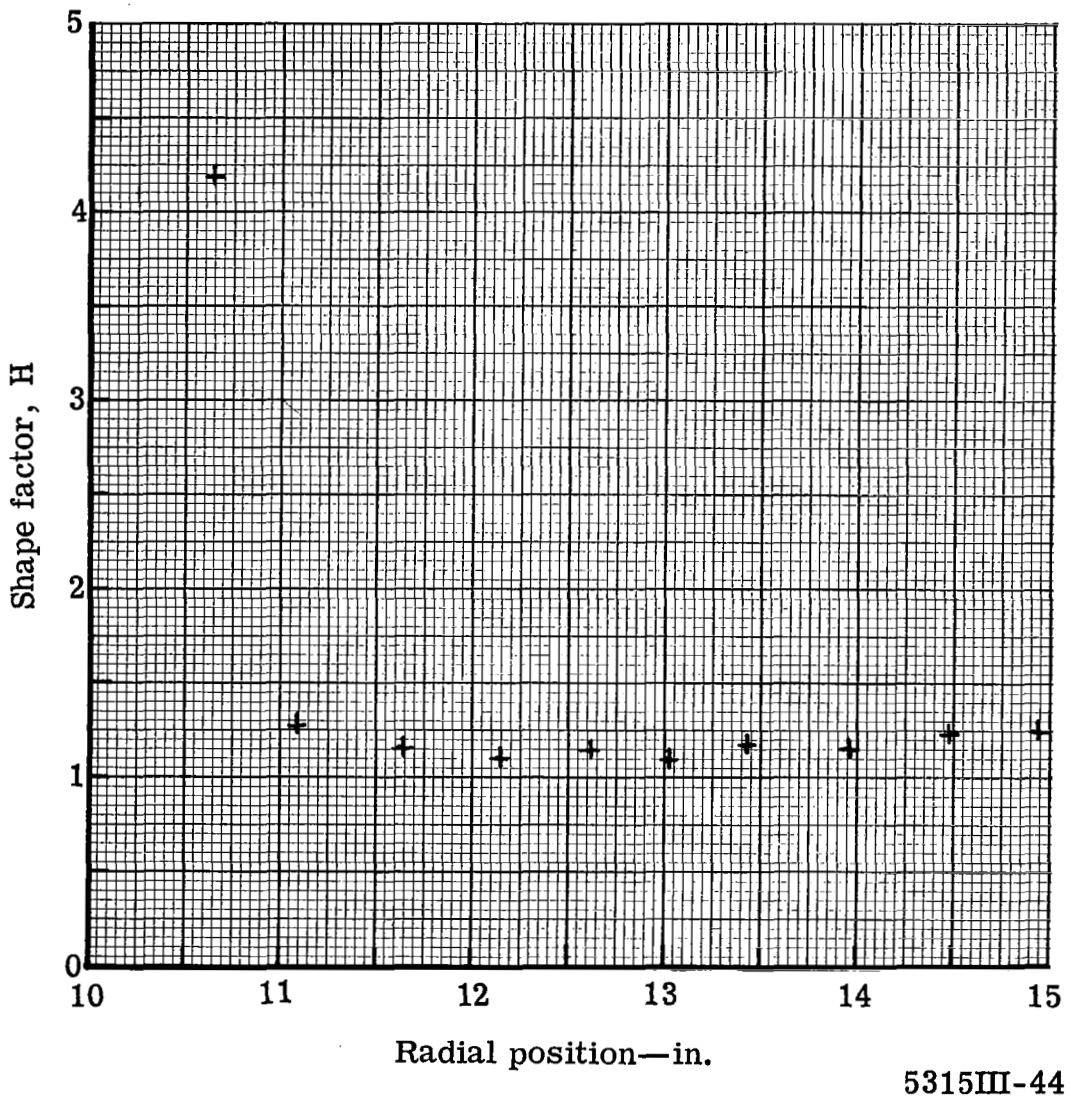

Figure 44. Tandem blade downstream wake survey-shape factor distribution at station 4.

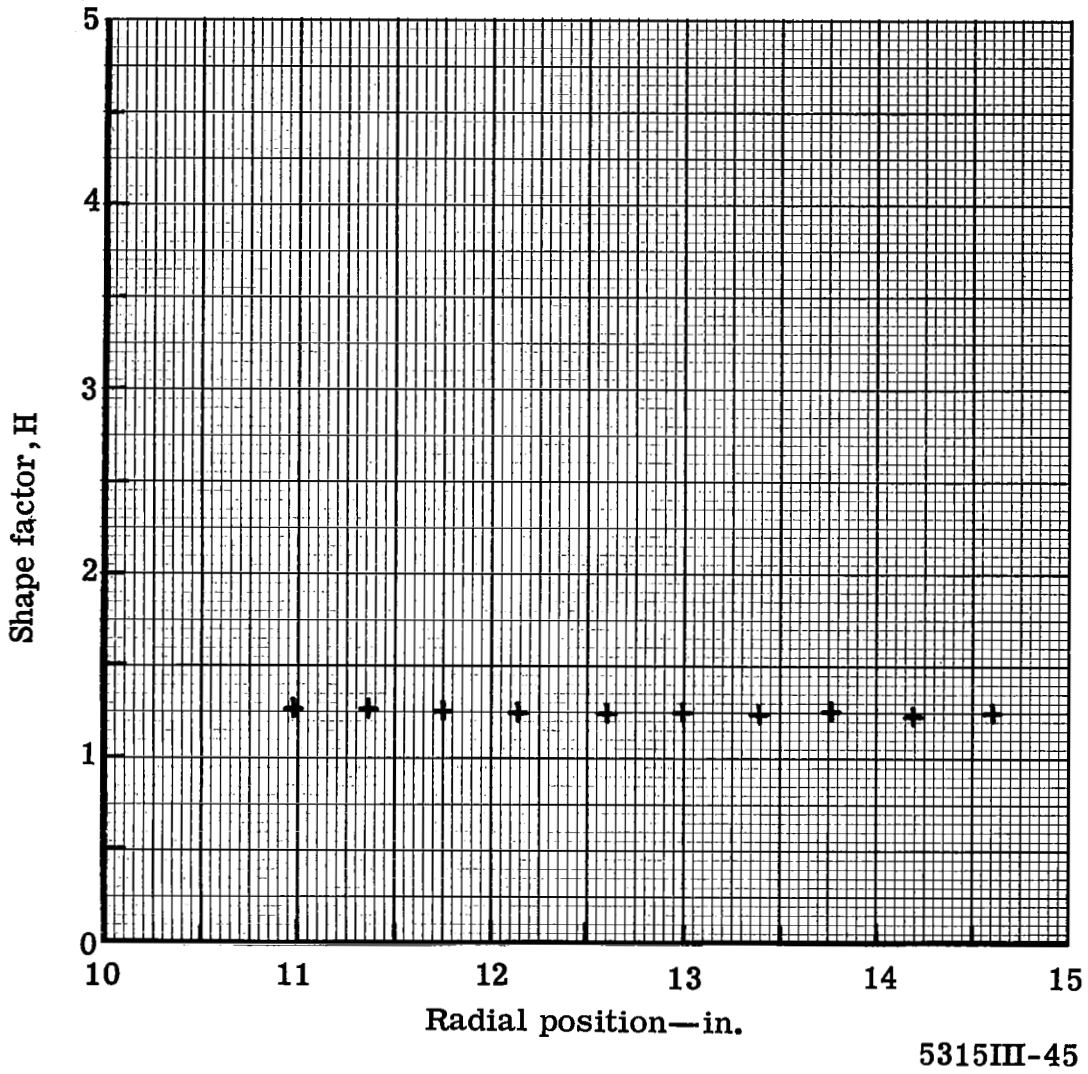

Figure 45. Plain blade downstream wake survey-shape factor distribution at station 4.